

# Measurements of $^{12}\text{C}$ ions fragmentation cross sections on thin targets with the FIRST apparatus.

Z. Abou-Haidar,<sup>a</sup> C. Agodi,<sup>b</sup> M.A.G. Alvarez,<sup>a</sup> T. Aumann,<sup>c</sup> F. Balestra,<sup>d</sup> G. Battistoni,<sup>e</sup> A. Bocci,<sup>a</sup> T.T. Böhlen,<sup>f</sup> A. Boudard,<sup>g</sup> A. Brunetti,<sup>h</sup> M. Carpinelli,<sup>h</sup> G.A.P. Cirrone,<sup>b</sup> M.A. Cortes-Giraldo,<sup>i</sup> G. Cuttone,<sup>b</sup> M. De Napoli,<sup>j</sup> M. Durante,<sup>c</sup> J.P. Fernández-García,<sup>k</sup> Ch. Finck,<sup>l</sup> B. Golosio,<sup>h</sup> E. Iarocci,<sup>m</sup> F. Iazzi,<sup>d</sup> G. Ickert,<sup>c</sup> R. Introzzi,<sup>d</sup> D. Juliani,<sup>l</sup> J. Krimmer,<sup>n</sup> A.H. Kummali,<sup>o</sup> N. Kurz,<sup>c</sup> M. Labalme,<sup>p</sup> Y. Leifels,<sup>c</sup> A. Le Fevre,<sup>c</sup> S. Leray,<sup>g</sup> F. Marchetto,<sup>q</sup> V. Monaco,<sup>o</sup> M.C. Morone,<sup>r</sup> D. Nicolosi,<sup>s</sup> P. Oliva,<sup>h</sup> A. Paoloni,<sup>t</sup> V. Patera,<sup>u</sup> L. Piersanti,<sup>u</sup> R. Pleskac,<sup>c</sup> N. Randazzo,<sup>j</sup> R. Rescigno,<sup>l</sup> F. Romano,<sup>v</sup> D. Rossi,<sup>c</sup> V. Rosso,<sup>w</sup> M. Rousseau,<sup>l</sup> R. Sacchi,<sup>o</sup> P. Sala,<sup>e</sup> S. Salvador,<sup>p</sup> A. Sarti,<sup>m</sup> C. Scheidenberger,<sup>c</sup> C. Schuy,<sup>c</sup> A. Sciubba,<sup>u</sup> C. Sfienti,<sup>x</sup> H. Simon,<sup>c</sup> V. Sipala,<sup>y</sup> E. Spiriti,<sup>z</sup> M. Toppi,<sup>aa</sup> S. Tropea,<sup>b</sup> M. Vanstalle,<sup>l</sup> and H. Younis<sup>bb</sup>

(The FIRST Collaboration)

(Dated: November 18, 2014)

A detailed knowledge of the heavy ions interaction processes with matter is of great interest in basic and applied physics. As an example, particle therapy and space radioprotection require highly accurate fragmentation cross section measurements to develop shielding materials, estimate acute and late health risks for manned missions in space and for treatment planning in particle therapy.

The FIRST (Fragmentation of Ions Relevant for Space and Therapy) experiment at the Helmholtz Center for Heavy Ion research (GSI) was designed and built by an international collaboration from France, Germany, Italy and Spain for studying the collisions of a  $^{12}\text{C}$  ion beam with carbon and gold thin targets. The experiment main purpose is to provide the first measurement of double differential cross section measurement of carbon ion fragmentation at energies that are relevant both for tumor therapy and space radiation protection applications. The SIS (heavy ion synchrotron) was used to accelerate the  $^{12}\text{C}$  ions at the energy of 400 MeV/u: this energy is particularly interesting for particle therapy applications, where  $^{12}\text{C}$  ions of such an energy are used for the treatment of deep seated tumors.

This paper presents the single differential fragmentation cross section, measured as a function of the fragments angle and kinetic energy. The impact on the applied fields relevant for such studies as well as the comparison with other published data in similar conditions will be also presented.

PACS numbers: Valid PACS appear here

---

<sup>a</sup> CNA, Sevilla, Spain

<sup>b</sup> Istituto Nazionale di Fisica Nucleare - Laboratori Nazionali del Sud, Italy

<sup>c</sup> GSI Helmholtzzentrum für Schwerionenforschung, Darmstadt, Germany

<sup>d</sup> Istituto Nazionale di Fisica Nucleare - Sezione di Torino, Italy; Dipartimento di Fisica, Politecnico di Torino, Italy

<sup>e</sup> Istituto Nazionale di Fisica Nucleare - Sezione di Milano, Italy

<sup>f</sup> European Organization for Nuclear Research CERN, Geneva, Switzerland; Medical Radiation Physics, Karolinska Institutet and Stockholm University, Stockholm, Sweden

<sup>g</sup> CEA-Saclay, IRFU/SPhN, Gif sur Yvette Cedex, France

<sup>h</sup> Istituto Nazionale di Fisica Nucleare - Sezione di Cagliari, Italy; Università di Sassari, Italy

<sup>i</sup> Departamento de Física Atómica, Molecular y Nuclear, University of Sevilla, 41080-Sevilla, Spain

<sup>j</sup> Istituto Nazionale di Fisica Nucleare - Sezione di Catania, Italy

<sup>k</sup> Departamento de Física Atómica, Molecular y Nuclear, University of Sevilla, 41080-Sevilla, Spain

<sup>l</sup> Institut Pluridisciplinaire Hubert Curien, Strasbourg, France

<sup>m</sup> Istituto Nazionale di Fisica Nucleare - Laboratori Nazionali di Frascati, Italy; Dipartimento di Scienze di Base e Applicate per l'Ingegneria, "La Sapienza" Università di Roma, Italy

<sup>n</sup> IPN-Lyon, Université de Lyon, Université Lyon 1, CNRS/IN2P3, Villeurbanne, France

<sup>o</sup> Istituto Nazionale di Fisica Nucleare - Sezione di Torino, Italy; Dipartimento di Fisica, Università di Torino, Italy

<sup>p</sup> LPC-Caen, ENSICAEN, Université de Caen, CNRS/IN2P3,

---

Caen, France

<sup>q</sup> Istituto Nazionale di Fisica Nucleare - Sezione di Torino, Italy

<sup>r</sup> Istituto Nazionale di Fisica Nucleare - Sezione di Roma Tor Vergata, Italy; Dipartimento di Biopatologia e Diagnostica per Immagini, Università di Roma Tor Vergata, Italy

<sup>s</sup> Dipartimento di Fisica, Università di Catania, Italy; Istituto Nazionale di Fisica Nucleare - Laboratori Nazionali del Sud, Italy

<sup>t</sup> Istituto Nazionale di Fisica Nucleare - Laboratori Nazionali di Frascati, Italy

<sup>u</sup> Istituto Nazionale di Fisica Nucleare - Sezione di Roma 1, Italy; Dipartimento di Scienze di Base e Applicate per l'Ingegneria, "La Sapienza" Università di Roma, Italy

<sup>v</sup> Istituto Nazionale di Fisica Nucleare - Laboratori Nazionali del Sud, Italy; Centro Studi e Ricerche e Museo Storico della Fisica "Enrico Fermi", Roma, Italy

<sup>w</sup> Dipartimento di Fisica, Università di Pisa, Italy; Istituto Nazionale di Fisica Nucleare - Sezione di Pisa, Italy

<sup>x</sup> Istituto Nazionale di Fisica Nucleare - Laboratori Nazionali del Sud, Italy; Medical Radiation Physics, Karolinska Institutet and Stockholm University, Stockholm, Sweden

<sup>y</sup> Istituto Nazionale di Fisica Nucleare - Sezione di Cagliari, Italy

<sup>z</sup> Istituto Nazionale di Fisica Nucleare - Laboratori Nazionali di Frascati, Italy; Istituto Nazionale di Fisica Nucleare - Sezione di Roma 3, Italy

<sup>aa</sup> Istituto Nazionale di Fisica Nucleare - Laboratori Nazionali di Frascati, Italy; Dipartimento di Fisica, Università di Roma Tor Vergata, Italy

<sup>bb</sup> Department of Physics COMSATS Institute of Information Technology, Islamabad Pakistan

## I. INTRODUCTION

The study of the mechanisms underlying the ion fragmentation in collisions at energies in the 10-1000 MeV/u range has been already object in the past of several experimental campaigns, either aiming at thin or thick target single or double differential cross section measurements [1–6]. Such measurements have been performed in different experimental conditions, covering in some cases only the very forward fragment emission region and in other cases few other fixed target angle configurations. Recently a double differential cross section measurement in thin targets has been performed using  $^{12}\text{C}$  ions of 95 MeV/u kinetic energy as projectiles, with an experimental setup able to cover a large angular range:  $0^\circ$  [7] and  $4^\circ$ - $45^\circ$  [8].

The interest in such measurements is driven by the possible use in space [9, 10] and particle therapy applications [11, 12] of an improved description of the heavy ions interactions with matter. In particular, for both applications, one of the most interesting ion type/energy range pair to be explored is  $^{12}\text{C}$  in the 200–1000 MeV/u range: cross section measurements using thin targets are needed in order to provide the missing information in the nuclear fragmentation databases, as NASA recently pointed out [13]. Deep seated tumors particle therapy with  $^{12}\text{C}$  ions is indeed spanning this energy range and a better understanding of the fragmentation of a carbon beam inside a patient will allow a better treatment planning.

The FIRST (Fragmentation of Ions Relevant for Space and Therapy) collaboration principal aim is to perform double differential cross section measurements (DDCS) using fully stripped  $^{12}\text{C}$  ions as projectiles on thin targets of carbon, gold and other materials in the energy range not yet covered by other experiments [14]. The data taking took place in the GSI laboratory (Darmstadt) in 2011 summer and about 25 (5) million events of collisions between a  $^{12}\text{C}$  ion beam with a thin carbon (gold) target were recorded.

The experimental setup, which included a trigger counter, a beam monitor, a vertex pixel detector, a plastic scintillator calorimeter and a time of flight wall (TW) made of plastic scintillators, is fully described in section II, together with the experiment Data Acquisition (DAQ) system. The performances obtained by the various subdetectors are outlined together with their calibration strategies and results.

Details on the data sample and on the MonteCarlo (MC) simulation are given in section III, the description of the global reconstruction algorithms that have been used to fully reconstruct all the fragments and particles traversing the detector in each event can be found in section IV, while the results are presented in section V. The studies performed to assess the systematic uncertainty are documented in section VI.

The impact of the obtained results for particle therapy applications, as well as some considerations about the future developments of the still ongoing data analysis are finally discussed in section VII.

## II. EXPERIMENTAL SETUP

Fragmentation cross sections are measured in FIRST using an experimental setup, already described in [14], that has been designed and optimized using a dedicated MC simulation. The schematic view of the FIRST experimental setup is shown in Fig.1, together with the axis orientation of the reference frame.

The detection of the incoming  $^{12}\text{C}$  ions has been accomplished by means of a Start Counter (SC), described in detail in § IIA, made of a thin layer of plastic scintillator whose geometry and read-out were optimized in order to maximize the counting efficiency while keeping the pre-target fragmentation as low as possible. The SC was used to trigger the data acquisition using a minimum bias strategy: whenever a  $^{12}\text{C}$  ion was detected inside the SC the event was acquired.

A pixel silicon detector (VTX), described in detail in § IIC, was placed just behind the target, allowing a precise reconstruction of the fragments produced in the target and their angle with respect to the incoming beam direction, as well as their production vertex. The technology adopted for the vertex detectors [15, 16] allowed to have the required efficiency with extra thin detection layers that minimized the out-of-target fragmentation of an elastically scattered  $^{12}\text{C}$  ion or other heavy fragments coming out from the target.

The long read-out time of the pixel detector, with an incoming beam rate in the 1-10 kHz range, required the development of a dedicated fast Beam Monitor (BM) detector, capable of resolving the event Pile Up (PU) ambiguity in the VTX by providing the position of the impinging  $^{12}\text{C}$  ion in the target. The technology chosen and the performances of such detector are presented in § IIB.

A plastic scintillator calorimeter (Kinetic ENergy and Time Resolution Optimized on Scintillator, KENTROS) has been used to detect fragments, mainly protons and heliums, emitted at large angles. This detector surrounds the target and vertex detector region covering the azimuthal angle (defined as the angle between the incoming  $^{12}\text{C}$  ion and the fragment direction) region between  $5^\circ$  and  $90^\circ$ . The results obtained in that region are not presented here and will be subject of a dedicated paper in the future, where a fully detailed description of the detector technology will be published.

The charged fragment momentum is computed by measuring the bending of the trajectory in the z-x plane induced by the magnetic field provided by the ALADIN magnet, whose description is reported in § IID.

The fragment identification and energy measurement are performed using scintillating detectors placed six meters away from the target region, arranged in a wall

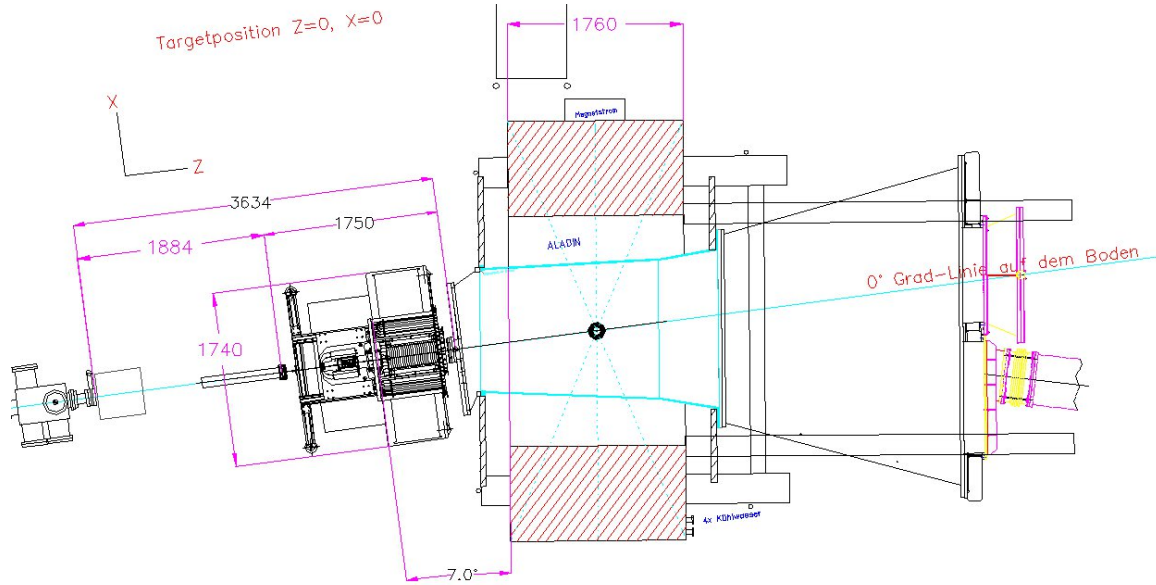


FIG. 1. Top view ( $x,z$  plane) of the FIRST experiment. From left to right: the beam pipe after the last collimator and the beam exit window; the table supporting the SC, the BM and the VTX detectors, enclosing the target holder; the KENTROS calorimeter, just before the magnet entrance window; the ALADIN magnet region; the TW detector at the right most position.

(TW), described in § II E. Together with the time of flight (ToF) measurement, TW provides the detected fragment coordinates and a measurement of the energy released inside the plastic scintillators: this information allows, when combined, a clean separation of fragments with different charge.

An additional detector, a large volume time projection chamber (TP-MUSIC IV [17]), was placed after the ALADIN magnet and before the TW, but could not be operated during the datataking; the experiment full simulation takes this detector into account in order to properly evaluate the material traversed by each fragment before reaching the TW and account for a possible secondary fragmentation.

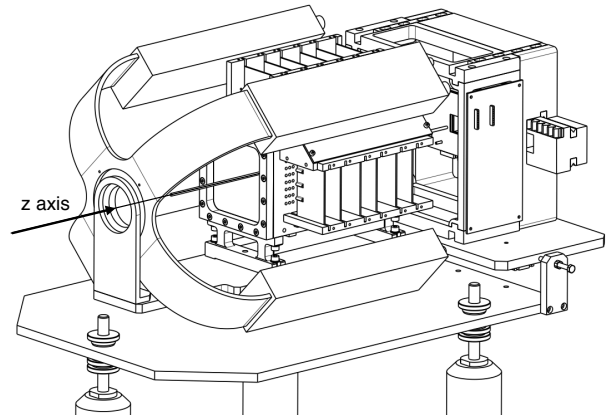


FIG. 2. Schematic view of the mechanical installation of SC and BM detectors. The picture shows the BM, with six wire planes on both  $xz$  and  $yz$  views, encapsulated by the SC mechanical structure. The four arms of the SC, holding the fibers and the PMTs used for the read-out can be clearly seen. The beam ( $z$ ) axis is also shown, crossing the SC and the BM in the middle of their entrance window. On the right, the aluminum box that encapsulates the target holder and the vertex detector is shown.

### A. Start Counter Detector

The SC detector is used in FIRST to provide a measurement of the total number of  $^{12}\text{C}$  ions used for the cross section evaluation and the trigger signal for the data acquisition system. The SC, shown in Fig. 2, also provides the reference time for all the other detectors, allowing the measurement of the drift time inside the BM, and of the fragment ToF using the TW information. The layout optimization, described in detail in [18], was hence performed carefully balancing the detector time resolution and the thickness minimization, in order to have a pre-target particle interaction probability that is less than 1% with respect to the on-target one.

The efficiency [18] showed an excellent stability during

the whole data taking, with a measured mean value of  $(99.7 \pm 0.15)\%$ . A good performance was also observed for the time resolution ( $\sigma_t$ ), with a measured average value of  $\sigma_t \approx (150 \pm 2)$  ps, where marginal fluctuations (maximum  $\approx 5$  ps) were observed.

## B. Beam Monitor Detector

173

174 The BM, described in detail in [18] and shown in Fig. 2,  
175 is a drift chamber designed for charged particles trajec-  
176 tory reconstruction. This detector is used to measure  
177 the ion impinging point on the target, a crucial informa-  
178 tion needed to address the pile up ambiguity in the VTX  
179 detector (see IIC 2).

180 The detector is made of twelve alternated horizontal  
181 (along x axis) and vertical (along y axis) wire planes.  
182 Each plane is composed of three rectangular cells cen-  
183 tered around the sense wires, with dimensions  $x(y) \times z =$   
184  $16 \text{ mm} \times 10 \text{ mm}$ , for a total of 36 cells/sense wires. The  
185 geometrical layout has been optimized in order to min-  
186 imize ions interactions with the wires still maintaining  
187 the required cell resolution. The twelve planes (six on  
188 each “view”) provide tracking redundancy and ensure a  
189 high tracking efficiency and an excellent spatial resolu-  
190 tion. The Beam Monitor was operated at 1.8 kV with an  
191 Ar/CO<sub>2</sub> (80%/20%) gas mixture, at atmospheric pres-  
192 sure.

193 The detector tracking algorithms have been presented  
194 elsewhere (in Ref. [18]): the tracking calibration has been  
195 performed using the tracks reconstructed in the VTX de-  
196 tector in a dedicated run in which the target was re-  
197 moved, thus allowing the detector alignment and the  
198 track intercalibration.

199 The chamber hit detection efficiency was measured to  
200 be  $\sim 97\%$  and was stable during the run as shown in Fig.3  
201 (black triangles) with the largest variation of  $\sim 3\%$ . The  
202 mean track spatial resolution at the chamber center was  
203 measured to be  $\sigma_x \approx 140 \mu\text{m}$ , with the dependence on the  
204 distance from the cell center described in [18].

## C. Vertex Detector

205

206 The main purpose of the vertex detector (VTX) is  
207 the trajectory and fragmentation vertex reconstruction of  
208 fragments produced in the target with the largest possi-  
209 ble angular coverage. The detector has been optimized in  
210 order to achieve an angular resolution better than  $\sim 0.3^\circ$   
211 for the two tracks separation.

212 The whole detector thickness could not exceed a few  
213 per cent of the target thickness to keep the probability  
214 of fragmentation inside the sensors at the few per cent  
215 level. A dynamic range from about two MIPs (Minimum  
216 Ionizing Particle), for the proton signal, to the two or  
217 three order of magnitude larger signal from low kinetic  
218 energy <sup>12</sup>C ions has also to be considered. To satisfy  
219 those requirements the MIMOSA26 (M26) pixel sensor  
220 has been chosen to equip the vertex detector with four  
221 sensor layers: the best compromise between the need of  
222 having a minimal track reconstruction redundancy and  
223 the sensor total thickness minimization.

224 M26 is a sensor chip developed by the Strasbourg group  
225 [15, 16] for high energy physics experiments. A sensitive

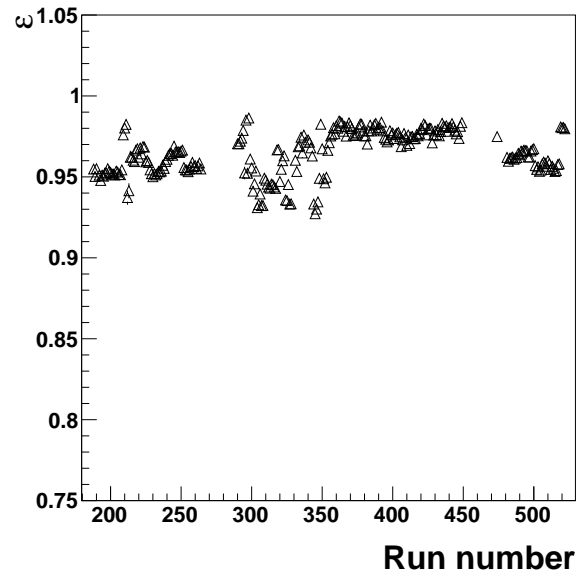


FIG. 3. Beam monitor tracking efficiency as a function of run number. The small fluctuations ( $\leq 3\%$ ) that can be observed against the mean value of 96.8% is due to the changes in the beam position, as well as to changes in the temperature and pressure of the gas mixture.

area of  $10.6 \text{ mm} \times 21.2 \text{ mm}$  is covered by 576 rows and 1152 columns of pixels with  $18.4 \mu\text{m}$  pitch with a read-out time of  $115.2 \mu\text{s}$  per frame.

230 All the pixels are read-out per column with a row  
231 read-out time of 200 ns. At the end of each column  
232 a discriminator is used to produce the input to the  
233 following zero suppression logic, that removes the empty  
234 pixel information and stores the data in two buffer  
235 memories. The data is thus sent off chip with two 80  
236 MHz serial differential outputs. Only four discriminator  
237 thresholds, each common to 288 discriminators, are  
238 provided.

239 To fit the experimental conditions a custom hous-  
240 ing board has been designed with two M26 glued on  
241 both sides of a square hole to obtain a sensitive area  
242 of  $\sim 2 \times 2 \text{ cm}^2$  including a small superimposition region  
243 essential to align all VTX sensors. The use of 1 mm  
244 thick PCB (Printed Circuit Board) and low profile com-  
245 ponents, allowing a distance of two consecutive boards of  
246 2 mm, produces an overall thickness of the four vertex  
247 stations of 12 mm, as shown in Fig. 4. In these condi-  
248 tions the angular coverage is  $\pm 40^\circ$ . Finally, the overall  
249 thickness of about  $50 \mu\text{m}$  per sensor, allows to minimize  
250 the lateral straggling of the impinging particles.

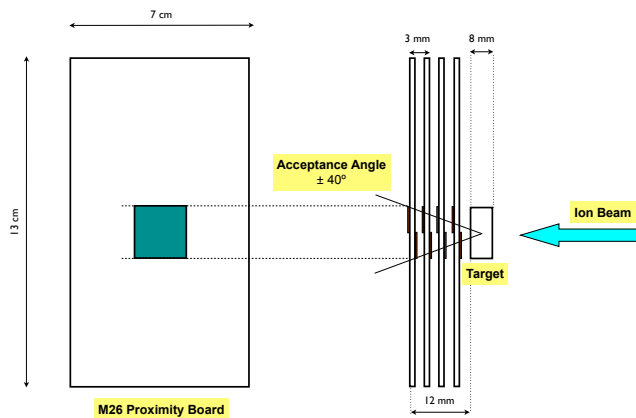


FIG. 4. Sketch of the VTX detector arrangement: the beam is impinging on 8 mm thick carbon target. Each of the four folowing PCBs is housing two sensors, one on each side, placed over a square hole (2 cm side length ) in the PCB itself.

### 1. Performances

The VTX detector data processing proceeds from the raw data file reading, from which a list of fired pixel is extracted, to the clusters reconstruction, centroid evaluation and combination into a list of tracks and vertices. A clustering algorithm is performed for each sensor to reconstruct the crossing point of the ionizing particles going through the M26 sensor. The algorithm is based on a recursive method looking for the next neighboring fired pixel and was able to reconstruct correctly the clusters with an efficiency higher than 99.9% [19].

Tracking reconstruction is based on standard algorithms tuned for the specific applications of CMOS sensors aiming for the reconstruction of a track going from a given plane to the next. Starting from the last plane and proceeding backwards with respect to the beam direction, a road to the position given by the BM extrapolation on the target is defined. Then all the available clusters on each plane within this road are identified and selected. The tracking reconstruction efficiency, evaluated on Monte Carlo simulation events (see § III) is  $98.7 \pm 0.1\%$ , with a measured proportion of fake tracks of  $1.99 \pm 0.01\%$  [19].

Two other different tracking approaches have been implemented and tested to assign a systematic uncertainty on the VTX tracking: one is based on the Hough transformation, while the other implements a different iterative procedure to scan the VTX planes to assign fired pixels to a given track in which consecutive planes are used. In the following, the first algorithm is used for track reconstruction since it is faster and exhibits a lower proportion of fake tracks.

The fragmentation vertices reconstruction is performed using an algorithm based on a probability distribution approach. Using the MC simulation a vertex recon-

struction efficiency of  $98.6 \pm 0.2\%$ , with a proportion of  $2.30 \pm 0.01\%$  fake vertices, has been estimated. The resolution of the vertex reconstruction, evaluated using Monte Carlo events, is better than  $10 \mu\text{m}$  in X and Y directions and better than  $50 \mu\text{m}$  in Z direction [19].

More than one  $^{12}\text{C}$  ion can impinge on the VTX detector during the M26 sensor integration time of  $115 \mu\text{s}$  (pile-up effect).

Using a Poisson distribution for pile-up events, with a  $\lambda$  parameter determined by data collected with the SC detector, it was found that only in  $(2.4 \pm 0.1)\%$  of the events, the vertex reconstruction algorithm could not disentangle the different vertices. From the data we obtain  $\lambda = 0.63 \pm 0.12$  where the uncertainty comes from the distribution of the  $\lambda$  values for different data samples. More details about the performance of the VTX detector can be found in reference [19].

The VTX alignment procedure is based on the minimization of the distance between the reconstructed clusters centroid and the intersection of the reconstructed tracks on the plane. The free parameters to be minimized are the displacement in the orthogonal plane with respect to the beam (X-Y plane) and the rotation around the beam axis (Z axis) for each sensor. Other rotations are neglected since the tracking procedure is less sensitive to them. The minimization is stopped once the variation of the displacement and angle is lower than a given value ( $\Delta X, \Delta Y < 5 \mu\text{m}$  and angle  $< 0.1^\circ$ ). Figure 5 shows the residuals obtained using  $^{12}\text{C}$  ions straight track events at 400 MeV/u for X and Y coordinates after the alignment procedure. The residuals are defined as the distance between the cluster positions and the fitted track line: their distribution was used to evaluate the resolution ( $\sigma$ ) of the tracking device by means of a Gaussian fit. The resolution in X and Y directions is better than  $\sigma = 5 \mu\text{m}$  and the fraction of tails outside a  $4\sigma$  window is smaller than 17%.

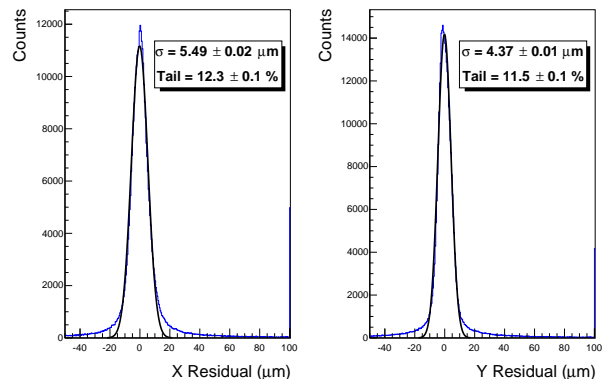


FIG. 5. Residuals obtained for reconstructed tracks in the X (left plot) and Y (right plot) directions. The data distribution is shown in blue, while the result of a Gaussian fit to the histogram is superimposed in black.

## 2. Matching with the BM

Since the tracks reconstructed by the VTX are the seed for the global track reconstruction algorithm (see § IV), it is crucial to preselect the tracks that belong to each event, getting rid of the piled-up tracks that may have been reconstructed. The ambiguities on which tracks belong to the current event can be resolved by using the information from the BM track, extrapolated to the target since the BM read-out time is fast enough to ensure that tracks belonging to different events cannot be mixed.

The track reconstructed in the BM is used to predict the impact point in the center of the target. The positions of the vertices reconstructed by the VTX for each event are compared with the position predicted by the BM and the closer vertex to the BM is selected as *matched vertex*. The impact of this selection on the final result and the relative systematic uncertainty on the cross section measurement is discussed in § VI.

The BM and VTX detectors were software aligned using calibration events taken without any target, with tracks traversing both detectors without any fragmentation or scattering. The alignment constants were tuned by minimizing the distance between the two predicted track intersections with a virtual plane in the target position (VTX - BM residual distribution) and the difference between the track parameters (like the angle with respect to the beam axis  $\theta$ ). The alignment result is shown in Fig. 6, where a bias in the VTX - BM residual distribution smaller than 200  $\mu\text{m}$  and a resolution of the order of 300  $\mu\text{m}$  for the X coordinate is shown, with similar results for the Y coordinate.

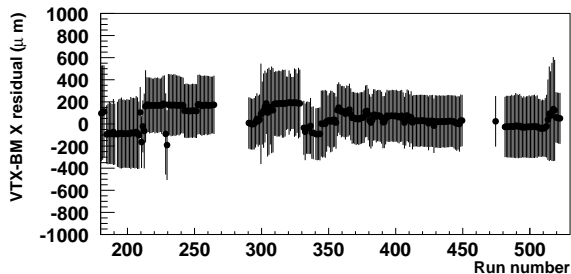


FIG. 6. Mean value of the residuals obtained for the X track at target position as measured using the BM and VTX detectors. The error bars are showing the sigma obtained from a fit done with a Gaussian PDF to the residual distribution and hence are representing the detector matching resolution.

## D. ALADIN Magnet

The p/Z ratio of charged fragments is reconstructed using the horizontal deflection in the Large Acceptance Dipole magnet (ALADIN). The magnetic field acts on the particles travelling in the magnet gap, operated in vacuum, that has an approximate volume of  $155(H) \times 421$

$50(V) \times 230(L) \text{ cm}^3$ . The magnet angular acceptance is limited to  $5.7^\circ$  by a circular collimator of 15 cm diameter positioned at 75 cm from the target.

The value of the magnet current has been chosen so that a non interacting beam particle crosses the central region of the TW, and it has been kept constant during the data taking within  $\pm 0.5\%$ . The corresponding deflection for a 400 MeV/u  $^{12}\text{C}$  ion is  $5.3^\circ$ .

The values of the magnetic field used in the reconstruction and simulation comes from interpolation of maps measured at GSI along the three coordinate axes on about 10 thousand grid points for different current values.

The actual current value used for the data analysis ( $\sim 680$  A) is determined with the MC by requiring that a beam particle crosses the TW in the same positions as measured in special runs with and without the magnetic field. The uncertainty on the magnet current and field scale is limited by the TW position resolution and estimated to be 2.5%. The uncertainty on the field scale and on the position of the magnet with respect to the rest of the apparatus is taken into account in the evaluation of the cross section measurement systematic errors.

## E. ToF-Wall Detector

The ToF-Wall (TW) detector has the aim of measuring the arrival time, the energy release and the impinging position of ions or fragments produced within the angular acceptance of the ALADIN entrance collimator ( $\lesssim 5^\circ$ ). Moreover, exploiting the information of energy release and arrival time, the TW allows the identification of the particles (incident  $^{12}\text{C}$  beam and fragments) arriving on it.

The detector, described in detail in [14], consists of two walls of BC-408 plastic scintillator slats (110 cm long, 1 cm thick) divided in 12 modules of 8 slats each. The detector is placed at a distance  $d \simeq 600$  cm from the target, along the trajectory of the  $^{12}\text{C}$  beam. The two walls are 8 cm far from each other.

At top and bottom ends of each slat, the signal of the impinging particle is read by two photomultiplier tubes (PMT) and then it is split and acquired by Fastbus Analog to Digital Converters (ADC) and, after being processed by Constant Fraction Discriminators (CFD) and digital delay modules, by Time to Digital Converters (TDC) for charge and time measurements, respectively, as shown in Fig. (7).

### 1. TW calibration

As mentioned before, the TW detector is fundamental in the experiment layout because it measures the horizontal and vertical coordinates ( $X$ ,  $Y$ ) of the impact

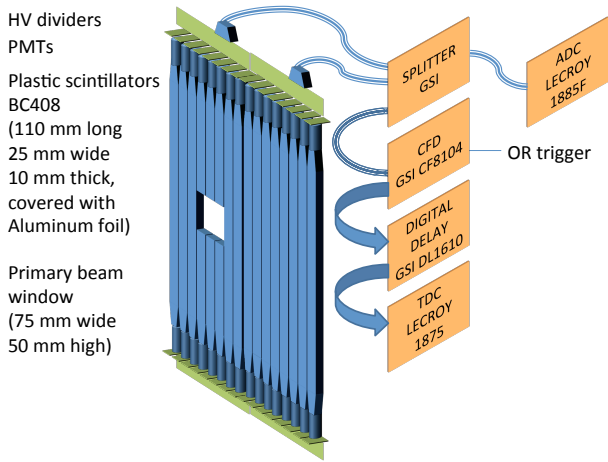


FIG. 7. Sketch of layout and connections of TW scintillator modules and of the read-out electronics with splitters, constant fraction discriminators (CFDs), digital delays, TDC and ADC boards.

point, the arrival time (ToF) and the energy released in the slats ( $E_{loss}$ ) of each impinging particle.

In particular, the coordinate in the horizontal plane is related to the slat number, which gives information on the  $X$  position of the particle and also on the fired wall (i.e.  $Z$  coordinate). The  $Y$  coordinate, instead, can be calculated in two ways: either starting from the difference of top and bottom TDC readings or by comparing the signals recorded in the two ADCs. The sum of top and bottom TDC readings is used to derive the particles ToF. Finally, the ADC channel measurements, providing information on the collected charge, allow to calculate the energy loss,  $E_{loss}$ , by the particle in the slat.

The calibrations of the quantities of interest have been performed exploiting particular data sets, called “sweep-runs”, collected without target, in which the beam conditions were known. In these runs the  $^{12}\text{C}$  ion beam (at 400 MeV/u) has been deflected, on the horizontal plane over all the slats, by varying the magnetic field.  $^{12}\text{C}$  ions flew at known energy – and thus at known velocity – on tracks which could be reconstructed by geometrical calculations. The hit coordinates ( $X, Y, Z$ ), ToF and  $E_{loss}$  are known on average for sweep-run hits: delays, constant factors and gains can thus be calibrated comparing the measured quantities, with the known values.

In addition to the ToF calibration, a data sample has been collected with dedicated runs in order to take into account the time dependence on the energy released by the fragments in each slat. A scan of the TW with the beam hitting an aluminium bar placed immediately before the scintillator front plane was performed. The time dependence on the released energy (time-walk effect) has been found to be  $< 0.5$  ns and thus has been neglected in the TW hit reconstruction.

While the ToF is known, since the path length for  $\text{C}^{512}$

projectiles with known energy (and velocity), deflected from the beam line on a given slat, can be computed through a geometrical reconstruction algorithm, the vertical coordinate can be calculated in two different ways, thanks to a redundancy in the information provided by TDCs and ADCs.

The first possibility is to calculate  $Y$  through the ADCs ( $Y_{ADC}$ ), assuming that an exponential attenuation is responsible of the signal decrease as a function of the length traversed along each slat and that the two photomultipliers can have different light gains. The calibration parameters have been measured by using the positions ( $Y$  coordinates) of the intercept between the VTX track extrapolation and the TW planes as a reference.

The second possibility is, instead, to use the TDC readings and the light speed in the scintillator ( $v_{sl}$ , slat dependent) to compute the  $Y$  coordinate ( $Y_{TDC}$ ): in the sweep-runs, on the horizontal plane taken as a reference, the vertical coordinate is known ( $Y = 0$ ). However this latter method suffer for a bigger uncertainty on the position and is only used for slats in which only one ADC was working.

After the pedestal subtraction, the ADC readings can be related to the scintillation light released by the particle by knowing the attenuation and the gain of the photomultipliers for each slat.

In sweep-runs the  $\text{C}$  ion energy is known and the energy loss can be evaluated according to the Bethe-Bloch formula. The computed  $E_{loss}$  is hence used to calibrate the TW detector parameters, taking also into account the non-linear response of plastic scintillators to the ionization density by applying the semi-empirical Birks’ formula [20], with parameters that are determined from the data.

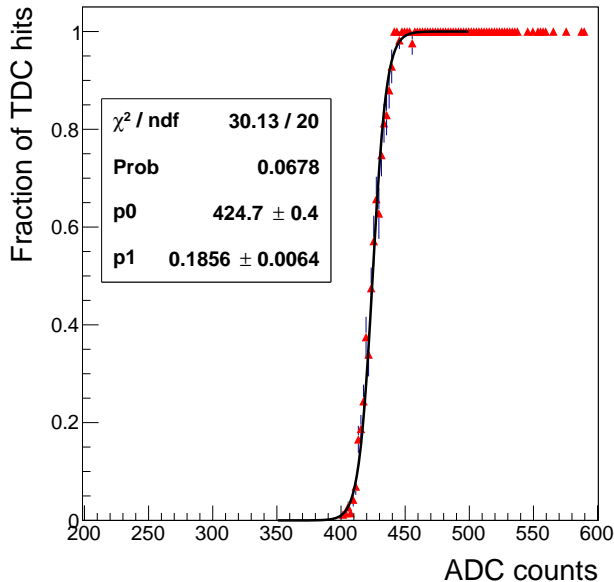
## 2. TW efficiency

The efficiency of the TW for proton detection is limited by the minimum signal needed to trigger the Constant Fraction Discriminators and to digitize the time information in the TDCs.

In order to simulate accurately this effect, for each TW channel the fraction of events with a detected TDC hit is studied as a function of the ADC counts after pedestal subtraction, as shown in Fig. 8 (for slat 33, top). The sharp transition from 0 to 1 (parameterized with a sigmoid fit) corresponds to the minimum ADC counts needed to trigger a TDC hit in each channel. The minimum released energy needed to trigger the TDC in each channel is estimated using the calibration parameters and Birks’ factors, and used in the Monte Carlo simulation to discard hits with an energy below threshold.

The minimum TW energy that can be detected in at least one of the two TDCs depends on the threshold values and on the  $Y$  position along the TW, due to the light attenuation along the slats. The energy threshold is below the energy released by a minimum ionizing particles,

513 excluding some regions, especially close to the impact  
 514 point of the carbon beam, where there is an efficiency  
 515 loss for protons of high kinetic energy.



516  
 517 FIG. 8. Fraction of events with a TDC hit as a function of  
 518 ADC counts for slat 33 of the TW.

### 519 3. TW Resolution

520 The resolutions in the TW reconstructed quantities<sup>543</sup>  
 521 ( $E_{loss}$ ,  $Y$ , ToF) are estimated by comparing the val-<sup>544</sup>  
 522 ues measured for hits in the two planes compatible with<sup>545</sup>  
 523 the same particle. The selection of the hits in different<sup>546</sup>  
 524 planes, optimized using the full Monte Carlo simulation,<sup>547</sup>  
 525 is based on the geometrical topology of the event and uses<sup>548</sup>  
 526 as input information the hits slat and  $Y$  positions. The<sup>549</sup>  
 527 resolutions are used for the tuning of the Monte Carlo  
 528 signal processing. <sup>550</sup>

529 The  $Y_{ADC}$  coordinate resolution was also evaluated<sup>551</sup>  
 530 using the uncertainty propagation, obtaining similar re-<sup>552</sup>  
 531 sults. The resolution we found, as expected, depends on<sup>553</sup>  
 532 the value of the vertical coordinate itself and it is shown<sup>554</sup>  
 533 as a function of the fragment energy, in Fig. 9 (top, right).<sup>555</sup>

534 The energy resolution is shown in Fig. 9 (bottom,<sup>556</sup>  
 535 right), for data and Monte Carlo as a function of the<sup>557</sup>  
 536 released energy. The ToF resolution shown in Fig. 9 (bot-<sup>558</sup>  
 537 tom, left) is about 800 ps while the  $Y_{TDC}$  resolution (top,<sup>559</sup>  
 538 left plot) is 8 cm and is nearly independent of the energy.<sup>560</sup>

### 539 F. Trigger and DAQ

540 The read-out of the detector electronics is performed<sup>564</sup>  
 541 on an event-by-event basis using the Multi Branch Sys-<sup>565</sup>  
 542 tem (MBS) [21], a general DAQ framework developed at<sup>566</sup>

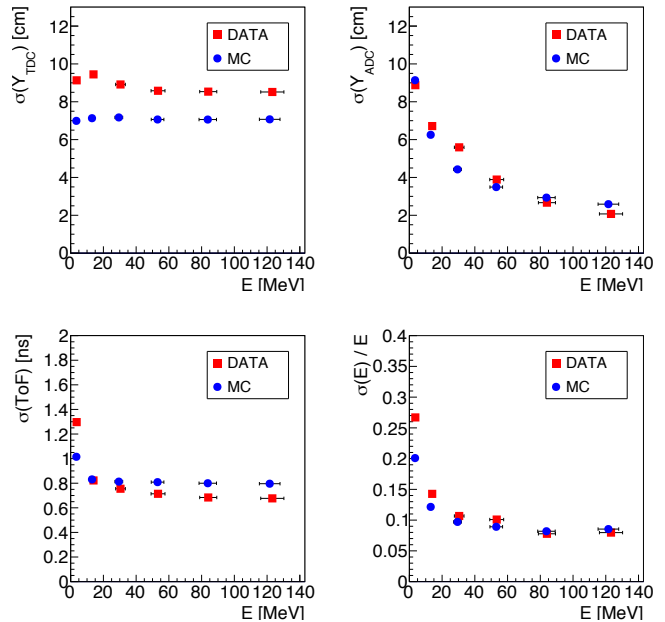


FIG. 9. Top left:  $Y_{TDC}$  resolution. Top right:  $Y_{ADC}$  resolution.  
 Bottom left: ToF resolution. Bottom right: energy resolution. All the distributions are shown for data (red squares) and MC (blue circles) event samples as a function of the released energy. A red line, showing a  $\propto 1/\sqrt{E}$  distribution is superimposed to the energy resolution distribution.

561 GSI. For each trigger, the MBS system handles the read-  
 out of the bus controllers hosted in different crates and  
 takes care of the trigger synchronization through signals  
 distributed on a common trigger bus. The event frag-  
 ments collected from all the individual controllers are  
 transmitted during the beam inter-spill period to a host  
 PC where the data merging and saving is performed.

562 The signals from single detectors are locally pro-  
 563 cessed with NIM electronics to generate trigger primi-  
 tives. The final trigger logic is implemented in a FPGA  
 programmable VME module (VULOM4 [22]), where the  
 local trigger primitives are combined in logic matrices.  
 The accepted triggers for different logical conditions  
 are propagated to the read-out electronics via the trigger bus.  
 Different trigger outputs are generated with downscale  
 factors or at random times for calibration purposes, while  
 the main physical trigger is based only on the signal from  
 the SC detector, thus providing an unbiased selection of  
 primary beam particles for the data analysis.

564 The typical beam rate during the data taking was  
 565 around 1 kHz, with instantaneous fluctuations related  
 566 to the spill structures provided by the SIS. The mean ac-  
 quisition rate was 150 Hz due to the dead times of the  
 single read-out nodes.



### III. DATA SAMPLE AND MC SIMULATION

The collected data sample of  $^{12}\text{C}$  ions collisions on the thin carbon target corresponds to 24 million unbiased triggers, while 4.5 million events have been collected with the thin gold target.

The simulation of the experiment is based on the general purpose Monte Carlo (MC) code Fluka [23, 24], used with the ‘‘HadronTherapy’’ physical model, which includes accurate simulation of non-elastic hadronic interactions at low energy and the evaporation and radioactive decays of heavy fragments.

The detector geometry and materials are modeled in a considerable detail, to properly evaluate the interactions in all the active detectors and the production of secondary particles in out-of-target fragmentation processes. The absolute positions of the detectors in the experimental area are fixed on the basis of the optical survey measurements results performed at the end of the data taking, complemented with alignment studies from the collected data.

The comparison of  $E_{\text{loss}}$ , ToF and  $Y$  coordinate measured from the TW detector for DATA and MC events in which a fragmentation occurred are shown in Fig. 10, where the distributions have been normalized in order to have the same integral. The fragmentation events are defined as those in which at least one vertex has been reconstructed in the VTX detector and more than one track is associated to it. The energy loss distribution for data is shown up to 100 MeV for fragments with  $Z$  ranging from one to five, since energy releases above 100 MeV are related to carbon ions. A detailed discussion on the charge identification of the fragments on the basis of energy loss and time of flight can be found in § IV A.

The pile-up of VTX tracks from different primary particles is simulated by adding additional tracks from events stored in a software FIFO, according to a trigger-conditioned Poissonian distribution determined from a data sample, with  $\lambda = 0.76$  (to account for the large pile-up condition measured in some data acquisition runs). The distributions of the number of vertices reconstructed with the VTX detector in data (for a large pile up run) and Monte Carlo simulation are compared in Fig. 11.

The detailed MC simulation of the geometry and of the detector response is needed to evaluate the acceptances and resolutions for the cross section measurement. For this purpose each reconstructed track is associated with a MC generated track and the reconstructed variables (kinetic energy, mass, charge, emission angle, momentum) are compared with the corresponding true value at generator level. A MC sample of 105 million events of  $^{12}\text{C}$  ions interactions with a carbon target has been used for this purpose: the tracking resolutions and efficiencies as well as a study of the combinatorial and misidentification background contamination in the fragments reconstruction have been performed on this sample (see § IV C).

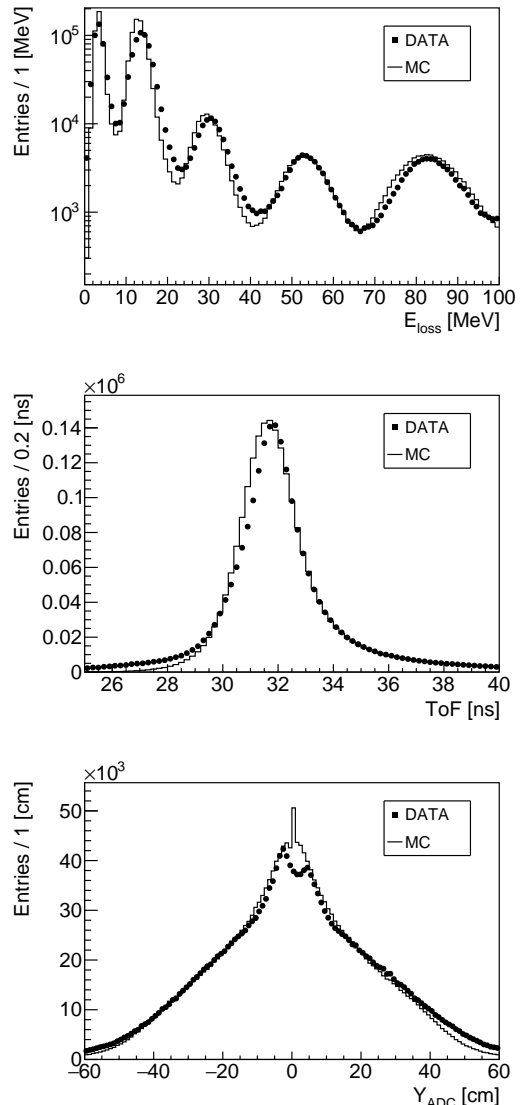


FIG. 10. Comparison of data and Monte Carlo distributions for TW reconstructed variables in fragmentation events. The data and MC spectra have been normalized in order to have the same integral.

### IV. GLOBAL RECONSTRUCTION

The fragment reconstruction in FIRST proceeds along two possible strategies, accordingly to their production angle: for small angle production (polar angle  $\theta$  less than  $\sim 6^\circ$ ) the fragment enters the ALADIN magnet region, where the momentum is computed measuring the bending in the  $x$ - $z$  plane, and is then detected by the TW; for large angle production ( $\theta$  larger than  $\sim 6^\circ$ ), the fragments cannot enter the magnet region and hence are detected by the KENTROS calorimeter.

The data analysis presented here covers only the small

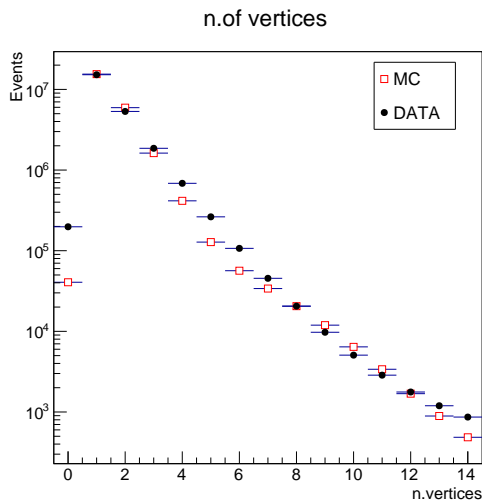


FIG. 11. Number of reconstructed vertices for DATA and MC. The MC distribution is normalized to the same number of entries of the data.

634 angle production region: fragments are reconstructed, in  
 635 this case, using an iterative procedure that matches the  
 636 VTX tracks and TW hits detected in each event. An ex-  
 637 ample of a fully reconstructed fragmentation event, in  
 638 which four fragments are produced at small angle, is  
 639 shown in Fig. 12. The fired BM wires/cells are high-  
 640 lighted in blue in the grayish box in the bottom left corner  
 641 of the picture. The KENTROS blue barrel and endcap  
 642 modules, surrounding the target/VTX region (not visible  
 643 in this global view scale) are shown as well. The  
 644 fragment tracks are represented as “dots” in space con-  
 645 necting the target origin position, and the relative four  
 646 fragment tracks in the VTX, with the four pairs of red  
 647 bands on the TW (two for each fragment as it traverses  
 648 both the front and the rear wall) representing the TW  
 649 slats that have been hit. The TW hits used to build the  
 650 track are shown as tiny spots in green.

651 The tracks bending happens in the grey box, repre-  
 652 senting the ALADIN magnet region: before and after  
 653 that region the magnetic field intensity is negligible and  
 654 the track trajectory is assumed to be a straight line.

### 655 A. Fragment charge identification

656 In order to fully reconstruct the fragment path and  
 657 reconstruct its momentum, the fragment charge has to  
 658 be measured. Two algorithms, based on the informations  
 659 from the TW and VTX detectors, have been developed.

660 The TW fragment charge identification is performed  
 661 using the measurements of  $E_{loss}$  and ToF. The TW per-  
 662 formances are good enough to allow the discrimination  
 663 of six spots in the  $E_{loss}$ -ToF plane, related to different  
 664 fragment charges as shown in figure 13. Each spot is fit-  
 665 ted with the Bethe-Bloch formula with  $Z$  corresponding

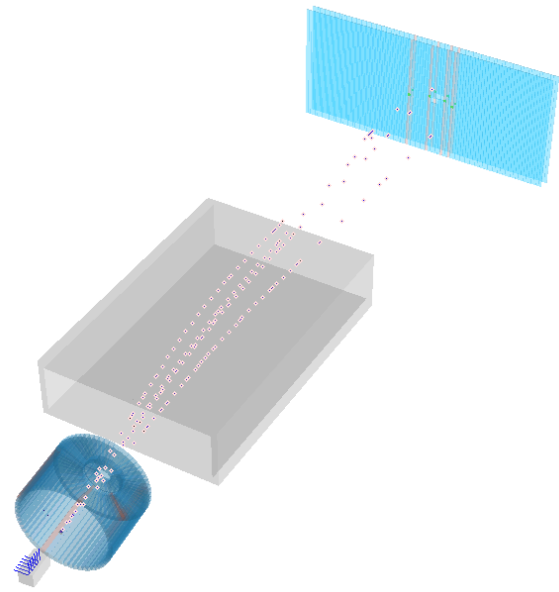


FIG. 12. 3D view of a fully reconstructed fragmentation event, with four fragments produced in the small angle region. Fragment tracks are built by pairing tracks reconstructed in the VTX detector (not shown in this figure, as the scale is too large) with the TW hits detected by the TW (shown in green in the top right light blue region that represents the TW). The tracks are represented as dots connecting the target/VTX region with the green dots on the TW. The magnet region is represented as a grey box between the KENTROS detector and the TW.

to the spot charge. Figure 13 shows the measured distributions for  $^{12}\text{C}$  ions on carbon target data, with Bethe-Bloch curves superimposed in black. For each point of the  $E_{loss}$ -ToF plane the minimum distance from each curve is calculated and six distributions of these distances are obtained. Performing a gaussian fit has been possible to get the mean value  $\mu_{dist}$  and the sigma  $\sigma_{dist}$  for each distance distribution. For each TW hit the identification algorithm computes the normalized distances  $\frac{distance - \mu_{dist}}{\sigma_{dist}}$  from the 6 different curves and assigns the charge corresponding to the one that minimizes it.

The VTX detector identification algorithm exploits the correlation between the size of the hit clusters and the fragment charge, as discussed in [25].

To benchmark the capabilities of the VTX detector, a clean sample of fragments whose charge was obtained from the TW detector has been used to estimate the

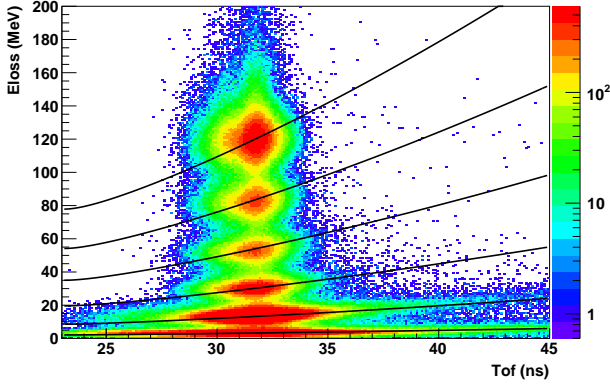
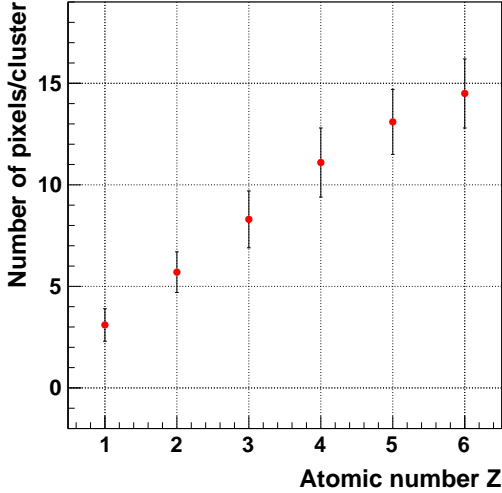


FIG. 13.  $E_{loss}$  vs ToF distribution

683 correlation with the cluster size. The result is shown in  
684 Fig. 14.



686 FIG. 14. Number of pixel associated to a given VTX cluster,  
687 as a function of the fragment charge as assigned from the TW  
688 detector reconstruction algorithm.

## 689 B. The global tracking algorithm

690 The global tracking algorithm implements three main  
691 steps.

- 692 1. First of all the event is pre-selected, applying sev-747  
693 eral filters: at least one hit on the TW and one748  
694 track in the VTX detector have to be reconstructed;749  
695 if more than one vertex is found in the VTX detec-750  
696 tor, the one closest to the BM extrapolated  $on$ -751  
697  $target$  position is taken as the true vertex for the752  
698 event under study, while the others are discarded753  
699 as PU vertices; only hits on the TW for which754

a charge assignment was possible are considered (see § IV A); only VTX tracks that are in the ALADIN magnet window entrance acceptance are considered.

- 700  
701  
702  
703  
704  
705  
706  
707  
708  
709  
710  
711  
712  
713  
714  
715  
716  
717  
718  
719  
720  
721  
722  
723  
724  
725  
726  
727  
728  
729  
730  
731  
732  
733  
734  
735  
736  
737  
738  
739  
740  
741  
742  
743  
744  
745  
746
2. For all the preselected events an iterative scan of the matching between VTX tracks and TW hits is performed, producing a list of global track candidates. Each track from the VTX is paired with each hit from the TW: clustering of TW hits is done afterwards, when the candidates are ranked and combined. For each candidate a minimization algorithm determines the optimal value of  $pc/Z$  and find the corresponding trajectory that matches the VTX track before the magnet and the TW position after the magnet.
3. The track candidates are finally combined and ranked accordingly to the VTX-TW matching quality in a final list to be used for the cross section measurements. To remove duplicates from the list referring to the same fragment to which more than one hit on the TW belongs, hits in the front and real planes that are compatible with the same particle according to geometrical and energetic criteria are clustered and treated in the reconstruction as a single hit. A scoring function to select the best candidates is then applied to the purged list.

A scoring algorithm combines the information from the VTX and the TW detectors to select the best track candidates. The measured quantities used to compute the weight for each VTX track / TW hit pair are: the difference between the particle charge as reconstructed from the VTX and from the TW detectors ( $\Delta_{Chg}$ ) and the difference between the Y position as extrapolated from the VTX and as measured with the TW ( $\Delta_Y$ ). The adopted scoring function is  $\sqrt{\Delta_{Chg}^2 \cdot Chg_W^2 + \Delta_Y^2 \cdot Y_W^2}$ . The  $Chg_W$  and  $Y_W$  weights have been tuned using the full MC simulation by minimizing the fraction of combinatorial tracks reconstructed. An example is shown in Fig. 15 for fragments with Z equal to one or two: the fraction of tracks in which the VTX track and the TW hits are not correctly paired with respect to the total number of reconstructed tracks is shown as a function of the charge weight  $Chg_W$ . The final  $Chg_W$  value chosen for the fragments reconstruction is eight.

For each selected final global track candidate, all the measured quantities are computed: the charge and the ToF are measured by the TW (for details see § IV A); the particle path (L) and the momentum over charge ratio ( $pc/Z$ ) are determined by the tracking algorithm, allowing a measurement of the fragment speed ( $\beta$  defined as  $L/ToF$ ); the mass is computed as  $\frac{p}{\gamma \cdot \beta}$ . The quantities used to build the single differential cross sections are respectively the fragment normalized kinetic energy ( $E_{kin}/u$ ), computed as the total fragment kinetic energy divided by the atomic number, and the fragment produc-

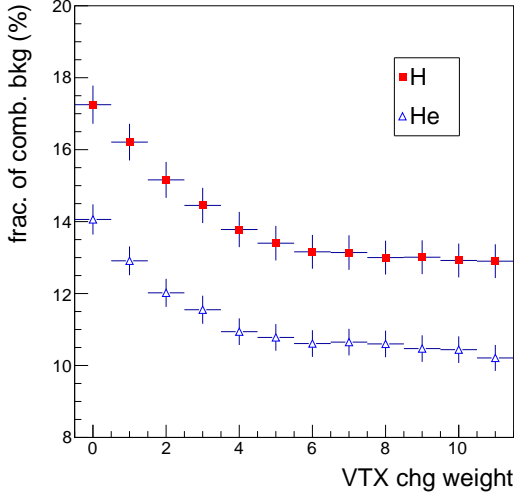


FIG. 15. Optimization of the  $Chg_w$  weight, based on the TW and VTX charge identification criteria, in the reconstruction. The fraction of tracks in which the VTX track and the TW hits are not correctly paired with respect to the total number of reconstructed tracks is shown as a function of the weight.

tion angle ( $\theta$ ) with respect to the beam axis, measured using the tracks reconstructed by the VTX detector.

### C. Tracking algorithm performances

The global reconstruction algorithms have been benchmarked against the full MC simulation (see § III). The angular and kinetic energy resolutions have been measured in order to evaluate any possible bias introduced by the reconstruction and to optimize the binning adopted for the SDCS measurement. The tracking efficiency and the background characterization have been performed on the full MC simulation as well. The observed discrepancies between the collected data and the MC simulation have been taken into account when assessing the systematic uncertainties on the result.

#### 1. Angular resolution

The angular resolution for the different fragments has been measured using fully reconstructed tracks from the full MC sample and it has been determined comparing the true generated fragment direction with the one reconstructed by the FIRST tracking algorithm. The resolution is found to be stable against the track angle, as shown in Fig. 16 with mean values that are in the range  $0.054^\circ$  (for carbons and borons) to  $0.076^\circ$  (for protons). Such numbers are entirely dominated by the intrinsic resolution of the VTX detector.

The reconstruction resolution with respect to the angle of the track generated inside the target is instead about

$0.1\text{--}0.15^\circ$ , depending on the fragment charge and energy and the multiple scattering undergone inside the target.

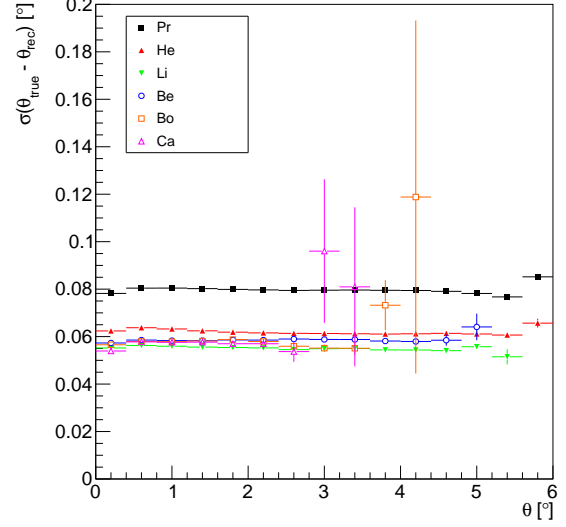


FIG. 16. Angular resolution as a function of the fragment azimuthal angle.

#### 2. Normalized kinetic energy resolution

The kinetic energy resolution ( $\sigma_{Ekin}$ ) has been measured using fully reconstructed tracks from the full MC sample.

Two main event categories are contributing to the  $\sigma_{Ekin}$  distribution: events in which the tracks are built using the correct combinations of VTX track and TW hits and events in which a wrong pair of VTX segments and TW hits was used. The reconstruction biases, as well as the resolutions, measured for the two categories are significantly different, as shown in Fig. 17 for fragments of charge 1.

The reconstruction efficiency and resolutions are estimated using the first sample of tracks, while the second sample is a combinatorial background to be subtracted on statistical bases from the sample of reconstructed tracks (see § IV D).

As an example, fig. 18 shows the resolution in the ratio of  $E_{kin}/u$  for tracks with right matches between VTX and TW hits of charge 1. The resolution increases at higher values of  $E_{kin}/u$  due to the reduced bending in the magnetic field and the limited spatial resolution of the TW detector.

The TW spatial granularity in the bending plane produces an increase of the mass resolution with the fragment charge, which ranges from  $0.05\text{--}0.2$  (MeV) for protons to  $0.3\text{--}0.5$  (MeV) for carbons.

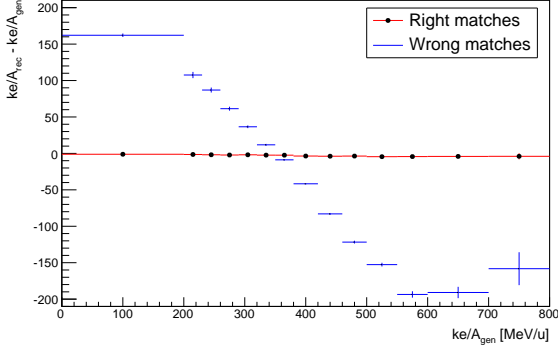


FIG. 17. Reconstruction biases (mean difference between generated and reconstructed values) in  $E_{kin}/u$  for tracks of charge 1 with correct and wrong VTX/TW matches.

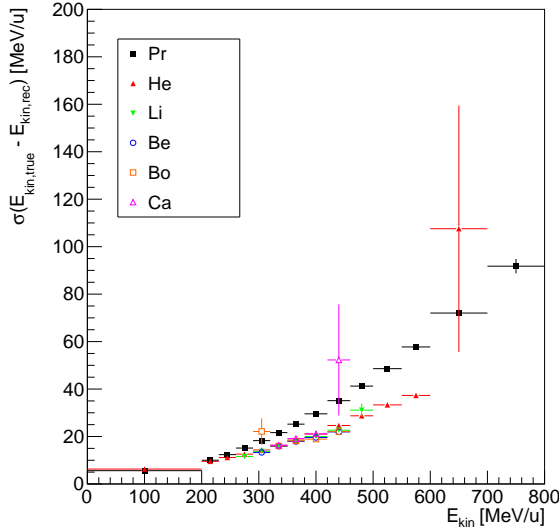


FIG. 18. Resolution in  $E_{kin}/u$  for tracks of charge 1 with right VTX/TW matches. The total error bars is twice the estimated resolution.

### 3. Tracking efficiency

The tracking algorithm efficiency has been evaluated using the full MC simulation sample available (see § III). For charged fragments emerging from the target region that are additionally required to point inside the geometrical acceptance of the ALADIN magnet ( $n_{PROD}$ ), we check if there is a reconstructed global track that is built using the true TW hit and VTX hits belonging to the true MC tracks under study ( $n_{REC}$ ). The efficiency is hence defined as  $\varepsilon_{trk} = n_{REC}/n_{PROD}$  and it is shown in Fig. 19, as an example, as a function of the measured angle  $\theta$ . The uncertainties shown are statistical only. The observed drop around  $5^\circ$  is due to the geometrical

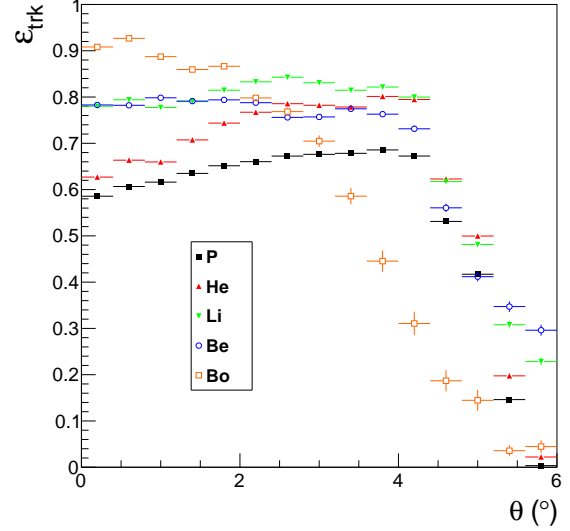


FIG. 19. Tracking efficiency ( $\varepsilon_{trk}$ ) as a function of fragment measured angle  $\theta$ .

acceptance of the ALADIN magnet entrance window. A similar distribution has been obtained as a function of the normalized kinetic energy and has been used to compute the SDCS as defined in Eq. 1.

### D. Combinatorial background evaluation

When pairing VTX tracks and TW hits to fully reconstruct the fragments as described in § IV B one has to account for the possibility that hits and tracks are not correctly matched or that background hits are paired to VTX tracks forming a random combination that is selected by the scoring algorithm. Such candidates are defined as “combinatorial background”, since it represents the effect of a fragment reconstruction that artificially pairs (combines) tracks and hits not belonging to the same fragment.

The mass spectra of such candidates have to be measured and properly taken into account when measuring the fragment production yields. Figure 20 shows, for the full MC sample, the mass spectra for two different kinetic energy ranges (200-230 MeV/u and 350-380 MeV/u) for fully reconstructed fragment candidates selected requiring that the VTX tracks and the TW hits used to build the track are belonging to two different particles.

In Fig. 20 the probability density function (PDF) used to model the combinatorial background in the unbinned likelihood fits used to measure the fragment production yields is shown, as a blue curve, superimposed to the reconstructed mass spectra (black dots). The PDF is built from the measured spectra using the one dimensional kernel estimation method [26] provided by the RooFit package [27].

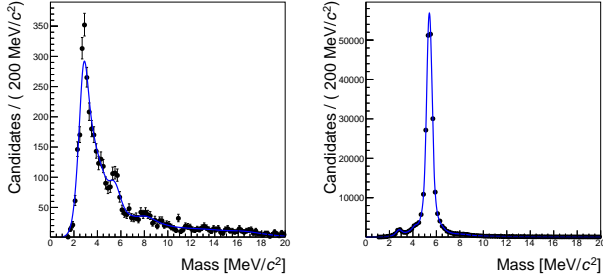


FIG. 20. Mass distribution for two different kinetic energy ranges, 200-230 MeV/u (left) and 350-380 MeV/u (right), for fully reconstructed fragment candidates with charge three.

Two different components can be identified in the combinatorial background mass spectra: a broad, nearly flat, component that is due to combination of background or noise hits and tracks and a peaking contribution, with peak position related to the charge assigned by the TW detector, that is due to tracks and hits from real fragments that are wrongly paired by the reconstruction algorithm.

The uncertainties related to the mass spectra, like the data/MC agreement and relative shape modifications, the different composition (in data and MC samples) of combinatorial background sample and relative weight of peaking and non peaking components have to be taken into account when fitting the data distributions. The treatment of such uncertainty and the contribution to the evaluation of the overall systematic uncertainty on the cross section measurement are discussed in § VI.

### E. Cross feed evaluation

The amount of cross feed between fully reconstructed fragments, due to the fragment misidentification on the TW, has been evaluated using the full MC sample.

The effect due to the wrong reconstruction of the fragment charge is shown clearly in Fig. 21, where the reconstructed mass spectrum is shown for the full MC sample, for events in which the reconstructed charge ( $Z_{ID}^{rec}$ , identified as outlined in § IV A) is equal to three. The total spectrum is shown in black (solid line). The contribution from the combinatorial background (see § IV D) is shown in red full squares, while the main signal contributions, respectively from  ${}^6\text{Li}$ ,  ${}^7\text{Li}$  and  ${}^8\text{Li}$  are shown as open marks (circle, square and triangle respectively). A clear contamination from  ${}^4\text{He}$  appears (in blue full triangles), under the  ${}^6\text{Li}$  peak: such contamination cannot be distinguished by the mass fit machinery (the slight shift in central mass value cannot be used in data due to the poor mass resolution) and hence has to be properly subtracted from the fitted yield ( $Y_i^{raw}$  in § V).

To compute the correction factors  $\varepsilon_i^{xf}$  that have to be applied to the  $Y_i^{raw}$  reconstructed yields for each isotope, we have analyzed the full MC sample, in bins of recon-

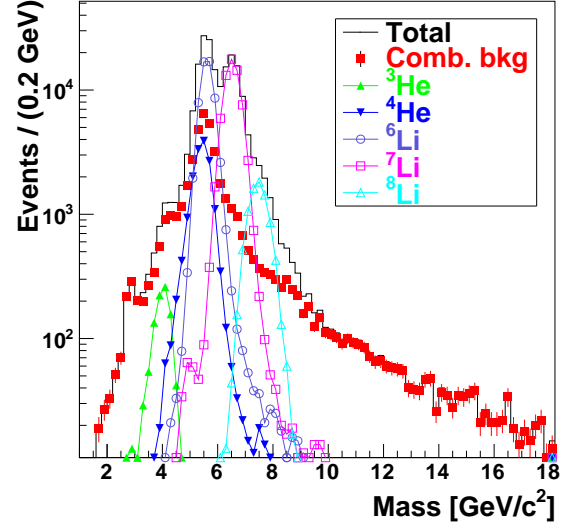


FIG. 21. Reconstructed mass spectrum for charge equal to three fragments (Li) from the full MC simulation sample. The black spectra is the total reconstructed spectrum. The red full squares are showing the combinatorial background contamination. The main signal contributions to the spectrum, respectively from  ${}^6\text{Li}$ ,  ${}^7\text{Li}$  and  ${}^8\text{Li}$  are shown as open marks (circle, square and triangle respectively). The cross feed background from  ${}^3\text{He}$  and  ${}^4\text{He}$  is shown in full triangles (green and blue, respectively).

structed angle and kinetic energy and identified and computed using the MC simulation the contaminations that cannot be subtracted or removed directly by the mass fit. While the absolute amount of a given contamination under a certain reconstructed peak depends clearly on the absolute fragmentation cross section implemented in the MC, the cross feed contamination is a relative correction that depends on the capability of the MC simulation to reproduce the ratio between the different cross sections.

We have therefore changed the  $\varepsilon_i^{xf}$  factors in order to take into account the difference in the integrated cross sections between data and MC: the change in the total cross section result for each isotope has been used to assign a systematic uncertainty (see § VI).

## V. CROSS SECTION MEASUREMENTS

The double differential cross section of fragment production as a function of the normalized kinetic energy ( $E$ ) or angle with respect to the beam axis ( $\theta$ ) is defined as:

$$\frac{d^2\sigma_i}{dE, d\theta} = \frac{Y_i}{N_{12C} \times N_{t,S} \times \Omega(ph.sp.) \times \epsilon_{trk}(E, \theta)} \quad (1)$$

where  $Y_i$  is the number of reconstructed fragments that have a given charge,  $N_{t,S}$  is the number of particles in the

target per unit surface,  $N_{12C}$  is the number of  $^{12}\text{C}$  ions impinging on the target,  $\epsilon_{trk}$  is the tracking reconstruction efficiency (defined in § IV C 3) and  $\Omega(ph.sp.)$  is a numerical factor accounting for the phase space relative to a given angular and kinetic energy bin.

The target particles per unit surface are measured, for the FIRST experimental setup, as  $N_{t,S} = \frac{\rho_{tgt} t N_a}{A}$  where the target density ( $\rho_{tgt}$ ) was measured to be  $4.25 \pm 0.01 \text{ g/cm}^3$ , the target thickness ( $t$ ) was  $8.07 \pm 0.01 \text{ mm}$  and  $N_a$  and  $A$  are the Avogadro number and the carbon atomic number respectively.

The phase space factor ( $\Omega(ph.sp.)$ ) is defined, accordingly to the angular ( $BW_\theta = \theta_{max} - \theta_{min}$ ) and kinetic energy range ( $BW_E = E_{max} - E_{min}$ ) of the selected fragments, as  $\Omega(ph.sp.) = (E_{max} - E_{min}) \cdot 2\pi \cdot (\cos(\theta_{min}) - \cos(\theta_{max}))$ . When the integrated SDCS are computed, either integrating on  $E$  or  $\theta$ , the corresponding  $\Omega(ph.sp.)$  is computed as either  $2\pi \cdot (\cos(\theta_{min}) - \cos(\theta_{max}))$  or  $(E_{max} - E_{min})$ . The size of  $BW_E$  and  $BW_\theta$  windows used to display the results have been chosen to be larger than the measured resolutions (see § IV) in order to limit the migrations of the fragments between the different bins.

The number of  $^{12}\text{C}$  ions impinging on the target ( $N_{12C}$ ) has been computed counting the physics unbiased triggers as defined in IIF. The occurrence of multiple  $^{12}\text{C}$  ions in a single event has been measured and found negligible in our data sample: for each trigger we count a single  $^{12}\text{C}$  ion crossing.

While the charge of each fragment is reconstructed using either the VTX or the TW detector, the production abundance of each fragment ( $Y_i^{raw}$ ), as well as the identification of different isotopes for each charge hypothesis is measured using the reconstructed mass spectra.

The  $Y_i^{raw}$  yields are measured using an unbinned maximum extended likelihood fit, performed using the RooFit ROOT toolkit [27]. An example of such fits, for fragments of different charge and selected in different  $E$  and  $\theta$  ranges, is shown in figure 22: superimposed to the data distribution (black dots), the total PDF is shown (in blue) while the signal PDF, modeling the various isotopes, is shown in red. A magenta dotted line shows the contribution from the combinatorial background.

The signal PDFs are gaussians, one gaussian for each isotope that is compatible with a given reconstructed charge, while the background PDFs, that are accounting for the combinatorial background that is the main contribution, have been described in § IV D and shown in Fig. 20.

Figure 22 shows the fit results for different charge and  $E, \theta$  ranges: the top row shows the invariant mass fits to the  $Z$  equal to one spectra in a given bin of angle (left) and energy (right), while the bottom row shows the same information for  $Z$  equal to three in different angle (left) and energy (right) bins.

The  $Y_i^{raw}$  yields from the fit have yet to be corrected for the cross feed contamination (see § IV E), while the combinatorial background is taken into account with a dedicated PDF. We compute the yields used for the cross

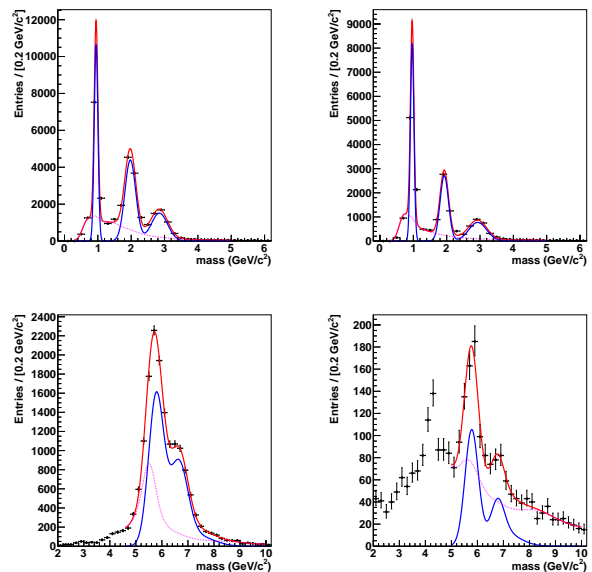


FIG. 22. Fit results for charge 1 (top) and 3 (bottom) mass spectra in different  $E, \theta$  ranges. The top left shows the invariant mass fits for charge equal to one fragments and angle between  $0.4^\circ$  and  $0.8^\circ$ , the top right for fragments with the same charge and a normalized kinetic energy in the range between  $200 \text{ MeV/u}$  and  $230 \text{ MeV/u}$ . The bottom left shows the invariant mass fits for charge equal to three fragments and angle between  $1.2^\circ$  and  $1.6^\circ$ , the bottom right fragments with the same charge and a normalized kinetic energy in the range between  $260 \text{ MeV/u}$  and  $290 \text{ MeV/u}$ .

section calculation as  $Y_i = \epsilon_i^{x,f} \times Y_i^{raw}$ .

The single differential cross section measured as a function of the angle with respect to the beam axis and of the normalized kinetic energy are shown, for the different measured charges, respectively in figures 23 and 24. The uncertainty shown in the plot is statistical only.

The histograms for each charge have been obtained by summing up all the non negligible contributions from different isotopes for a given charge: for example, the result shown in the first bin of the  $Z$  equal to one is obtained summing the proton, deuteron and triton yields as measured from the fit shown in Fig. 22 (top left).

## VI. SYSTEMATIC CHECKS

Several systematic checks have been performed on the cross section measurement in order to assess the impact of the limited knowledge of different crucial analysis items and to account for the use of MC related quantities and for possible discrepancies between data and MC.

The analysis has been redone several times, changing the reconstruction algorithms, MC models, measurement strategies, and we have finally assigned to each measurement a systematic uncertainty by looking at the results measured spread (RMS). In the following we will refer to

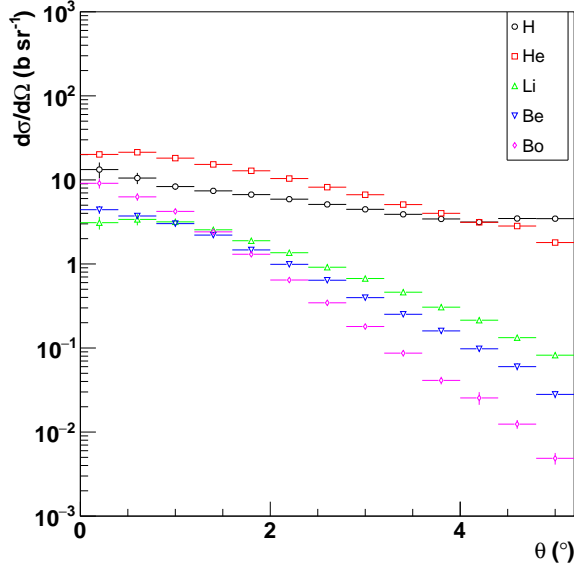


FIG. 23. SDCS of different charge ( $Z$ ) fragment production, as a function of the fragment angle with respect to the beam axis, computed using Eq. 1.

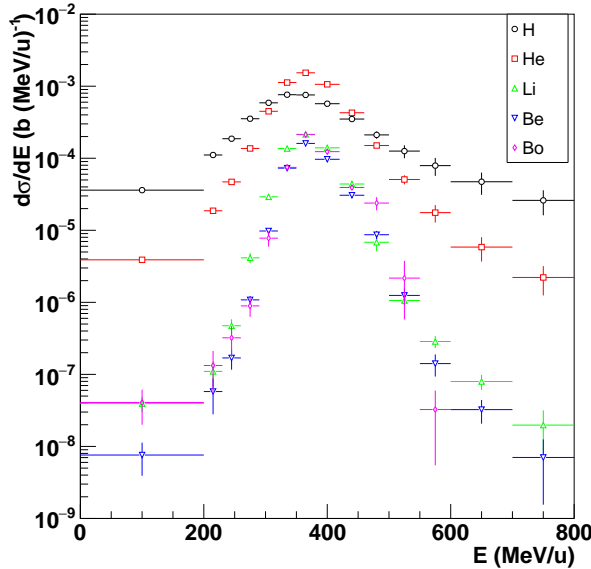


FIG. 24. SDCS of different charge ( $Z$ ) fragment production, as a function of the fragment normalized kinetic energy, computed using Eq. 1.

a signal, we have re-computed the analysis efficiencies and cross sections, considering only events in which both TDCs gave a signal. The difference observed is significant only for protons and is shown, in red full topside down triangles in Fig. 25 (*SCC* spectrum).

The analysis has also been redone by changing both the scoring function (using only the  $\Delta_Y$  weight) and disabling the TW hits clustering algorithm. The result, for protons is shown in Fig. 25 (*Cls/Sco* spectrum) in blue empty circles. The analysis has also been redone dropping the requirement of a matched BM track with the VTX detector (Fig. 25, *BM mat* spectrum) and by changing the VTX tracking algorithm, in order to test the VTX tracking robustness when removing the BM information for the track reconstruction (Fig. 25, *VTX trk* spectrum). The results fluctuation has been used to compute the systematic uncertainty to be quoted on the *Default* result.

To evaluate the impact on the knowledge of the TW position with respect to the general FIRST reference frame, we have redone the analysis changing the TW position in the reconstruction algorithm about  $\pm 1$  cm (position resolution from the survey performed after the data taking). The result is shown in Fig. 25 spectra labeled as *TW pos+(-)*. A similar study has been done changing the magnet position and the magnetic field scale within the experimental precisions. **The syst study is under way, plots/results will be added ASAP.**

In order to account for possible differences between data and MC and to take into account the induced bias on the measurement of  $Y^{raw}$  we have recomputed the yields after changing the combinatorial mass model PDF by reducing the value of the  $\rho$  parameter (promoting the detail preservation over the PDF smoothness). **The syst study is under way, plots/results will be added ASAP.**

The systematic checks include the evaluation of the MC simulation impact on the estimate of the cross feed correction that is used to correct the  $Y^{raw}$  yields as presented in § IV E. The correction factors computed from the MC simulation have been rescaled in order to take into account the difference between the ratio of fragments production cross sections in data and MC: the analysis has been redone with the new factors and the difference with respect to the *Default* is used to compute a systematic uncertainty. **The syst study is under way, plots/results will be added ASAP.**

## VII. CONCLUSIONS

The FIRST experiment performed a measurement of SDCS, as a function of fragment angles and kinetic energies, studying a data sample of several million collisions of  $^{12}\text{C}$  ions impinging on a thin (8 mm) carbon target. This is the first measurement ever made, in such experimental configuration, performed with an ion energy of 400 MeV/u, that is particularly interesting for particle therapy and space applications.

the result obtained following the prescriptions and strategies outlined in the previous sections as *Default* result. An important contribution to the systematic uncertainty quoted for the proton cross section, comes from the modeling of the TW hit detection efficiencies: we have done the analysis considering and neglecting proton events in which both TDCs, for the different TW slats, gave a signal. While the *Default* result contains the events in which only one TDC, for a given slat, gave



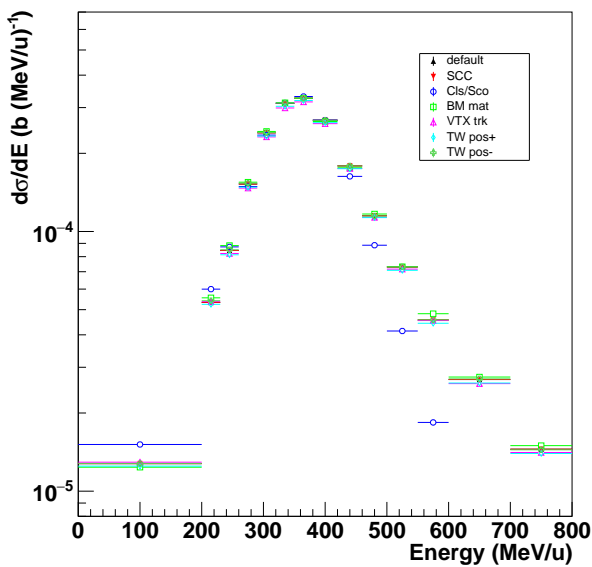
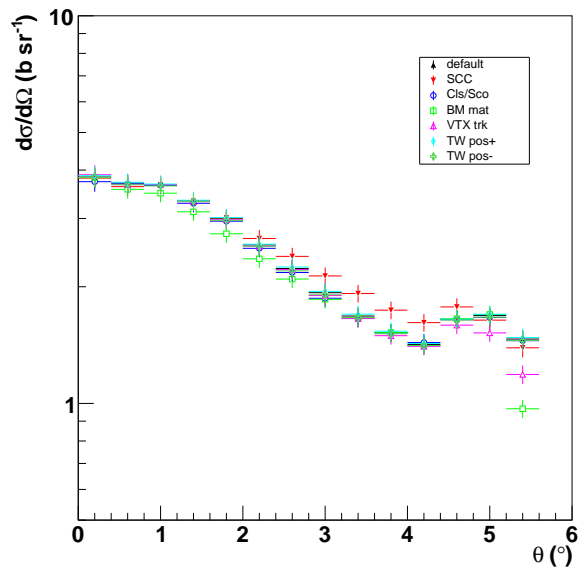


FIG. 25. Effect of systematic checks on the production cross section of  $^1\text{H}$  fragments. The production cross section obtained changing the analysis strategy, algorithm and cuts, as discussed in the text, is shown.

The result presented here, while being systematically dominated, achieves an unprecedented precision on the single differential cross sections of carbon ions on a thin carbon target. While this study covers only a limited angular range (up to five degrees), reports only the single differential cross sections on the carbon target, a refined analysis, to be performed in the full angular range accessible to the experiment, as a function of  $E$  and  $\theta$  and including the gold target sample, is in preparation.

## ACKNOWLEDGEMENTS

We would like to acknowledge M. Arba, L. La Delfa and M. Tuveri (INFN Sez. Cagliari), M. Anelli, S. Cerioni, G. Corradi, D. Riondino and R. Rosellini (INFN, LNF), M. Capponi and A. Iacofano (INFN, Sez. Roma3) for the technical design and mechanical work on the Interaction Region and Filippo Bosi (INFN Sez. Pisa) for his help and suggestions. We also acknowledge Dr. Håkan T. Johansson for the invaluable help in setting up the trigger. This work has been supported by the European Community FP7 - Capacities, contract ENSAR n 262010. This work was also supported by Junta de Andalucía and the Spanish Ministerio de Ciencia e Innovación Contracts P07-FQM-02894, FIS2008-04189 and FPA2008-04972-C03.

- [1] M. De Napoli *et al.*, “Carbon fragmentation measurements and validation of the GEANT4 nuclear reaction models for hadrontherapy”, *PHYSICS IN MEDICINE AND BIOLOGY* **57** (2012) 7651-7671
- [2] M. De Napoli *et al.*, “Carbon Fragmentation Cross Sections for Hadrontherapy and Space Radiation Protection” *Nuclear Data Sheets Volume 119*, pages 273-276 (2014)
- [3] C. Zeitlin *et al.*, “Fragmentation of 14-N, 16-O, 20-Ne and 24-Mg Nuclei at 290 to 1000 MeV/nucleon”, *Phys. Rev. C* **83** (2011) 034909
- [4] C. Zeitlin *et al.*, “Fragmentation cross sections of 290-MeV/nucleon and 400-MeV/nucleon C-12 beams on elemental targets”, *Phys. Rev. C* **76** (2007) 014911.
- [5] T. Toshito *et al.*, “Measurements of total and partial charge-changing cross sections for 200- to 400-MeV/nucleon C12 on water and polycarbonate”, *Phys. Rev. C* **75** (2007) 054606.
- [6] N. Matsufuji *et al.*, “Spatial fragment distribution from a therapeutic pencil-like carbon beam in water”, *Phys. Med. Biol.* **50** (2005) 3393.

- 1111 [7] J. Dudouet *et al.*, “Zero-degree measurements of C12<sub>142</sub>  
1112 fragmentation at 95 MeV/nucleon on thin targets”, Phys<sub>143</sub>  
1113 Rev. C **89**, (2014) 064615. 1144
- 1114 [8] J. Dudouet *et al.*, “Double-differential fragmentation<sub>145</sub>  
1115 cross-section measurements of 95 MeV/nucleon 12G<sub>146</sub>  
1116 beams on thin targets for hadron therapy,” Phys. Rev. C<sub>147</sub>  
1117 **88**, 024606 (2013). 1148
- 1118 [9] M. Durante and F. A. Cucinotta, “Physical basis of ra<sub>149</sub>  
1119 diation protection in space travel.”, Rev. Mod. Phys. **83**<sub>150</sub>  
1120 (2011) 1245-1281 1151
- 1121 [10] L. Ziwei, “Determination of important nuclear fragmen<sub>152</sub>  
1122 tation processes for human space radiation protection.”<sub>153</sub>  
1123 Phys. Rev. C **75** (2007) 034609 1154
- 1124 [11] D. Schardt, T. Elsässer and D. Schulz-Ertner, “Heavy<sub>155</sub>  
1125 Ion Tumor Therapy: Physical and Radiobiological Ben<sub>156</sub>  
1126 efits.”, Rev. Mod. Phys. **82** (2010) 383-422 1157
- 1127 [12] J. S. Loeffler and M. Durante, “Charged particle<sub>158</sub>  
1128 therapy—optimization, challenges and future directions.”<sub>159</sub>  
1129 Nat. Rev. Clin. Oncol. **10** (2013) 411-424 1160
- 1130 [13] J. W. Norbury, J. Miller, A. M. Adamczyk, L. Heilbronn<sub>161</sub>  
1131 L. W. Townsend, S. R. Blattnig, C. J. Zeitlin (2012)<sub>162</sub>  
1132 “Nuclear data for space radiation”. Radiat. Meas., **47**(5)<sub>163</sub>  
1133 315363. doi:10.1016/j.radmeas.2012.03.004 1164
- 1134 [14] R. Pleskac *et al.*, “The FIRST Experiment at GSI”, Nucl<sub>165</sub>  
1135 Instr. Methods in Phys. Res. A, Vol. 687 (2012) 130. 1166
- 1136 [15] <http://www.iphc.cnrs.fr/-CMOS-ILC-.html> 1167
- 1137 [16] Ch.Hu-Guo *et al.*, Nuclear Inst. and Methods in Physics<sub>168</sub>  
1138 Research, Vol. 623, (2010), p. 480-482 1169
- 1139 [17] C. Sfienti *et al.*, Proceedings of the XLI International<sub>170</sub>  
1140 Winter Meeting on Nuclear Physics, Bormio, Italy,  
1141 (2003), p. 323.
- [18] Z. Abou-Haidar *et al.*, “Performance of upstream interac-  
tion region detectors for the FIRST experiment at GSI,”  
JINST **7**, P02006 (2012).
- [19] R. Rescigno *et al.*, “Performance of the reconstruction  
algorithms of the FIRST experiment Pixel Sensors Ver-  
tex detector”, Nuclear Inst. and Methods in Physics Re-  
search A, Vol. 767, (2014), p. 34-40
- [20] J. B. Birks, “Scintillations from Organic Crystals: Spe-  
cific Fluorescence and Relative Response to Different Ra-  
diations”, Proc. Phys. Soc. A **64** 874 (1951)
- [21] H. G. Essel, N. Kurz, IEEE Transactions on Nuclear Sci-  
ence NS-47 (2) (2000) 337.
- [22] [https://www.gsi.de/informationen/wti/ee/elekt\\_entwick\\_lung/vulom.m.e.html](https://www.gsi.de/informationen/wti/ee/elekt_entwick_lung/vulom.m.e.html)
- [23] G. Battistoni *et al.*, “The FLUKA code: Description and  
benchmarking”, Proceed. of the Hadronic Shower Sim-  
ulation Workshop2006, (2007), aIP ConferenceProceed.  
896(2007)3149.
- [24] A. Ferrari, P. R. Sala, A. Fassó, J. Ranft, “FLUKA: a  
multi particle transport code”, Tech. Rep. CERN-2005-  
10, INFN/TC05/11, SLAC-R-773 (2005).
- [25] E. Spiriti *et al.*, “The FIRST experiment: interaction  
region and MAPS vertex detector”, Nucl. Phys. B (Proc.  
Suppl.) **215** (2011) 157161.
- [26] K. S. Cranmer, “Kernel Estimation in High-Energy  
Physics”, Computer Physics Communications **136**:198-  
207,2001. e-Print Archive: hep ex/0011057
- [27] W. Verkerke and D. P. Kirkby, “The RooFit toolkit for  
data modeling,” arXiv:physics/0306116.

TABLE I. Angular Differential Cross Section ( $b \text{ sr}^{-1}$ )

$\theta$ (deg)	$^1\text{H}$ $d\sigma/d\Omega(b \text{ sr}^{-1})$	$^2\text{H}$ $d\sigma/d\Omega(b \text{ sr}^{-1})$	$^3\text{H}$ $d\sigma/d\Omega(b \text{ sr}^{-1})$	$^3\text{He}$ $d\sigma/d\Omega(b \text{ sr}^{-1})$	$^4\text{He}$ $d\sigma/d\Omega(b \text{ sr}^{-1})$	$^6\text{He}$ $d\sigma/d\Omega(b \text{ sr}^{-1})$
0.2(0.2)	3.8 (0.23)	7.3 (2.3)	2.8 (0.5)	1.7 (0.38)	18 (1.2)	0.051 (0.076)
0.6(0.2)	3.7 (0.2)	4.5 (1.3)	2.6 (0.33)	1.8 (0.18)	19 (1.2)	0.28 (0.088)
1(0.2)	3.7 (0.2)	2.7 (0.41)	2.1 (0.28)	1.9 (0.19)	16 (1)	0.13 (0.066)
1.4(0.2)	3.3 (0.19)	2.3 (0.22)	1.9 (0.28)	1.9 (0.19)	13 (0.75)	0.17 (0.06)
1.8(0.2)	3 (0.18)	2.2 (0.16)	1.6 (0.17)	1.8 (0.16)	11 (0.57)	0.21 (0.033)
2.2(0.2)	2.6 (0.16)	2 (0.13)	1.5 (0.088)	1.6 (0.14)	8.7 (0.46)	0.12 (0.019)
2.6(0.2)	2.2 (0.14)	1.8 (0.11)	1.2 (0.074)	1.4 (0.095)	6.7 (0.35)	0.087 (0.0087)
3(0.2)	1.9 (0.13)	1.5 (0.085)	1 (0.079)	1.3 (0.081)	5.3 (0.28)	0.045 (0.0085)
3.4(0.2)	1.7 (0.12)	1.4 (0.084)	0.82 (0.075)	1.2 (0.068)	3.9 (0.21)	0.0087 (0.0072)
3.8(0.2)	1.5 (0.11)	1.1 (0.081)	0.72 (0.073)	0.99 (0.058)	3 (0.16)	3.4e-08 (0.0027)
4.2(0.2)	1.4 (0.1)	1 (0.076)	0.64 (0.078)	0.82 (0.046)	2.3 (0.12)	0.012 (0.0048)
4.6(0.2)	1.6 (0.1)	1.1 (0.064)	0.69 (0.069)	0.77 (0.044)	2.1 (0.12)	0.023 (0.0034)
5(0.2)	1.7 (0.1)	1.1 (0.068)	0.7 (0.06)	0.46 (0.03)	1.3 (0.078)	0.017 (0.0033)
5.4(0.2)	1.5 (0.2)	0.89 (0.13)	0.61 (0.099)	0.13 (0.01)	0.34 (0.022)	0.006 (0.0019)
5.8(0.2)	0.0091 (0.0037)	0.006 (0.0026)	0.003 (0.0015)	0.0014 (0.00055)	0.0018 (0.00069)	0.00046 (0.00025)
$\theta$ (deg)	$^6\text{Li}$ $d\sigma/d\Omega(b \text{ sr}^{-1})$	$^7\text{Li}$ $d\sigma/d\Omega(b \text{ sr}^{-1})$	$^8\text{Li}$ $d\sigma/d\Omega(b \text{ sr}^{-1})$	$^7\text{Be}$ $d\sigma/d\Omega(b \text{ sr}^{-1})$	$^9\text{Be}$ $d\sigma/d\Omega(b \text{ sr}^{-1})$	$^{10}\text{Be}$ $d\sigma/d\Omega(b \text{ sr}^{-1})$
0.2(0.2)	1.4 (0.31)	0.99 (0.46)	0.51 (0.17)	1.8 (0.25)	0.94 (0.37)	2 (0.56)
0.6(0.2)	1.5 (0.16)	1.6 (0.49)	0.18 (0.032)	1.4 (0.14)	1.2 (0.3)	1.2 (0.37)
1(0.2)	1.5 (0.22)	1.4 (0.41)	0.17 (0.036)	1.3 (0.087)	0.93 (0.16)	0.82 (0.19)
1.4(0.2)	1.3 (0.21)	0.96 (0.32)	0.18 (0.033)	1.1 (0.075)	0.69 (0.11)	0.46 (0.11)
1.8(0.2)	1 (0.16)	0.61 (0.23)	0.19 (0.046)	0.82 (0.049)	0.39 (0.063)	0.29 (0.053)
2.2(0.2)	0.8 (0.17)	0.42 (0.22)	0.15 (0.041)	0.61 (0.038)	0.33 (0.031)	0.049 (0.03)
2.6(0.2)	0.49 (0.13)	0.39 (0.13)	0.017 (0.014)	0.43 (0.026)	0.13 (0.031)	0.085 (0.018)
3(0.2)	0.36 (0.11)	0.31 (0.1)	0.01 (0.025)	0.28 (0.017)	0.072 (0.014)	0.048 (0.02)
3.4(0.2)	0.14 (0.077)	0.33 (0.078)	0.0017 (0.014)	0.18 (0.011)	0.044 (0.012)	0.029 (0.016)
3.8(0.2)	0.09 (0.039)	0.22 (0.033)	0.0017 (0.014)	0.13 (0.009)	0.014 (0.005)	0.017 (0.0055)
4.2(0.2)	0.065 (0.024)	0.15 (0.024)	0.0082 (0.004)	0.079 (0.0055)	0.017 (0.0039)	0.002 (0.0046)
4.6(0.2)	0.047 (0.017)	0.09 (0.019)	0.0013 (0.0019)	0.049 (0.0042)	0.012 (0.0028)	0.0024 (0.00074)
5(0.2)	0.036 (0.0079)	0.038 (0.0059)	0.0071 (0.0016)	0.021 (0.0022)	0.0077 (0.0017)	0.00056 (0.00024)
5.4(0.2)	0.008 (0.002)	0.0066 (0.0019)	0.00049 (0.001)	0.0046 (0.00069)	0.00058 (0.00062)	4.4e-11 (8.3e-05)
5.8(0.2)	0.0002 (0.00014)	0.0001 (9.4e-05)	5.1e-05 (6.4e-05)	6e-05 (7e-05)	3e-05 (4.8e-05)	3e-05 (4.8e-05)
$\theta$ (deg)	$^8\text{Bo}$ $d\sigma/d\Omega(b \text{ sr}^{-1})$		$^{10}\text{Bo}$ $d\sigma/d\Omega(b \text{ sr}^{-1})$		$^{11}\text{Bo}$ $d\sigma/d\Omega(b \text{ sr}^{-1})$	
0.2(0.2)	0.16 (0.073)		4.9 (2)		4.2 (1.3)	
0.6(0.2)	0.023 (0.018)		0.35 (1.5)		6.1 (1.5)	
1(0.2)	0.063 (0.012)		1.8 (0.69)		2.4 (0.74)	
1.4(0.2)	0.052 (0.025)		0.2 (0.32)		2.2 (0.36)	
1.8(0.2)	0.06 (0.014)		0.81 (0.31)		0.45 (0.29)	
2.2(0.2)	0.033 (0.013)		0.11 (0.072)		0.52 (0.093)	
2.6(0.2)	0.037 (0.0057)		0.083 (0.089)		0.23 (0.095)	
3(0.2)	0.016 (0.0032)		0.16 (0.055)		0.0063 (0.054)	
3.4(0.2)	0.014 (0.0037)		0.052 (0.024)		0.018 (0.021)	
3.8(0.2)	0.0041 (0.0023)		0.035 (0.0056)		0.0042 (0.0025)	
4.2(0.2)	0.0041 (0.0014)		0.018 (0.008)		0.0047 (0.0044)	
4.6(0.2)	0.0058 (0.0013)		0.0053 (0.0019)		0.0017 (0.0015)	
5(0.2)	0.0011 (0.00076)		0.0037 (0.00089)		0.00036 (0.00055)	
5.4(0.2)	0.00093 (0.00029)		0.00062 (0.00022)		0.00093 (0.00029)	
5.8(0.2)	0 (0)		0 (0)		0 (0)	

TABLE II. Energy Differential Cross Section (b MeV/nucl<sup>-1</sup>)

Energy (MeV/u)	<sup>1</sup> H $d\sigma/dE(b\text{ MeV/u}^{-1})$	<sup>2</sup> H $d\sigma/E(b\text{ MeV/u}^{-1})$	<sup>3</sup> H $d\sigma/E(b\text{ MeV/u}^{-1})$	<sup>3</sup> He $d\sigma/E(b\text{ MeV/u}^{-1})$	<sup>4</sup> He $d\sigma/E(b\text{ MeV/u}^{-1})$	<sup>6</sup> He $d\sigma/E(b\text{ MeV/u}^{-1})$
100(100)	1.28e-05 (9.01e-07)	1.73e-05 (1.03e-06)	5.43e-06 (3.14e-07)	2.10e-06 (8.90e-08)	1.58e-06 (5.94e-08)	1.94e-07 (4.14e-08)
215(15)	5.33e-05 (2.60e-06)	3.88e-05 (1.46e-06)	1.71e-05 (9.07e-07)	1.01e-05 (4.26e-07)	7.84e-06 (4.23e-07)	9.26e-07 (2.05e-07)
245(15)	8.45e-05 (2.72e-06)	6.37e-05 (2.99e-06)	3.88e-05 (3.15e-06)	2.21e-05 (7.29e-07)	2.33e-05 (1.06e-06)	1.67e-06 (3.70e-07)
275(15)	1.52e-04 (3.57e-06)	1.21e-04 (6.54e-06)	8.25e-05 (6.26e-06)	4.79e-05 (1.71e-06)	8.56e-05 (4.01e-06)	2.51e-06 (8.11e-07)
305(15)	2.40e-04 (5.12e-06)	1.98e-04 (9.93e-06)	1.54e-04 (8.01e-06)	1.01e-04 (3.45e-06)	3.37e-04 (1.78e-05)	4.33e-06 (1.30e-06)
335(15)	3.11e-04 (6.42e-06)	2.52e-04 (8.74e-06)	2.02e-04 (5.36e-06)	1.62e-04 (5.46e-06)	9.27e-04 (3.59e-05)	1.52e-05 (3.75e-06)
365(15)	3.26e-04 (6.29e-06)	2.41e-04 (7.71e-06)	1.95e-04 (3.39e-06)	1.99e-04 (4.55e-06)	1.31e-03 (2.39e-05)	1.78e-05 (5.38e-06)
400(20)	2.68e-04 (4.51e-06)	1.78e-04 (6.94e-06)	1.34e-04 (3.28e-06)	1.62e-04 (3.80e-06)	9.03e-04 (1.80e-05)	8.02e-06 (1.18e-06)
440(20)	1.79e-04 (5.71e-06)	1.07e-04 (8.13e-06)	7.35e-05 (4.58e-06)	8.04e-05 (1.64e-06)	3.52e-04 (6.35e-06)	1.61e-06 (5.01e-07)
480(20)	1.15e-04 (9.36e-06)	6.62e-05 (9.51e-06)	3.96e-05 (5.80e-06)	3.29e-05 (9.43e-07)	1.17e-04 (8.67e-06)	4.79e-07 (2.77e-07)
525(25)	7.30e-05 (1.10e-06)	3.84e-05 (8.72e-06)	2.45e-05 (6.12e-06)	1.19e-05 (8.12e-07)	3.81e-05 (6.63e-06)	5.82e-07 (2.31e-07)
575(25)	4.56e-05 (9.69e-06)	2.43e-05 (6.89e-06)	1.73e-05 (5.58e-06)	1.14e-05 (4.53e-06)	6.26e-06 (3.48e-06)	3.27e-07 (1.43e-07)
650(50)	2.69e-05 (7.16e-06)	1.67e-05 (5.46e-06)	1.02e-05 (3.54e-06)	4.55e-06 (2.22e-06)	1.16e-06 (4.29e-07)	1.15e-07 (5.37e-08)
750(50)	1.45e-05 (4.42e-06)	9.45e-06 (3.39e-06)	6.03e-06 (2.13e-06)	1.73e-06 (9.14e-07)	5.65e-07 (2.01e-07)	4.40e-08 (1.81e-08)
Energy (MeV/u)	<sup>6</sup> Li $d\sigma/E(b\text{ MeV/u}^{-1})$	<sup>7</sup> Li $d\sigma/E(b\text{ MeV/u}^{-1})$	<sup>8</sup> Li $d\sigma/E(b\text{ MeV/u}^{-1})$	<sup>9</sup> Be $d\sigma/E(b\text{ MeV/u}^{-1})$	<sup>9</sup> Be $d\sigma/E(b\text{ MeV/u}^{-1})$	<sup>10</sup> Be $d\sigma/E(b\text{ MeV/u}^{-1})$
100(100)	2.37e-08 (6.73e-09)	1.58e-08 (5.45e-09)	2.04e-11 (1.81e-10)	5.17e-09 (2.98e-09)	1.74e-09 (1.71e-09)	6.66e-10 (1.04e-09)
215(15)	5.78e-08 (2.69e-08)	5.34e-08 (2.65e-08)	1.05e-09 (3.36e-09)	4.63e-08 (2.53e-08)	8.98e-09 (1.01e-08)	5.25e-09 (7.64e-09)
245(15)	4.14e-07 (9.19e-08)	1.22e-07 (4.08e-08)	4.52e-09 (7.12e-09)	1.13e-07 (4.01e-08)	3.78e-08 (2.14e-08)	2.10e-08 (1.55e-08)
275(15)	2.85e-06 (3.30e-07)	6.53e-07 (3.84e-07)	5.30e-07 (1.89e-07)	9.17e-07 (1.39e-07)	1.77e-07 (5.23e-08)	4.97e-09 (9.08e-09)
305(15)	1.40e-05 (1.02e-06)	1.27e-05 (1.30e-06)	7.59e-07 (4.14e-07)	6.69e-06 (8.07e-07)	2.49e-06 (5.02e-07)	3.40e-07 (7.54e-07)
335(15)	6.39e-05 (2.83e-06)	5.88e-05 (6.05e-06)	9.40e-06 (1.26e-06)	3.83e-05 (2.81e-06)	1.10e-05 (5.78e-06)	2.33e-05 (6.32e-06)
365(15)	9.46e-05 (4.73e-06)	9.45e-05 (8.58e-06)	1.69e-05 (2.16e-06)	7.92e-05 (2.72e-06)	6.94e-05 (1.36e-05)	1.31e-05 (1.64e-05)
400(20)	6.32e-05 (6.30e-06)	6.12e-05 (7.68e-06)	1.38e-05 (2.30e-06)	5.94e-05 (2.03e-06)	3.13e-05 (2.65e-06)	8.63e-06 (1.14e-06)
440(20)	1.54e-05 (2.87e-06)	2.57e-05 (5.07e-06)	1.75e-06 (8.06e-07)	2.09e-05 (6.42e-07)	5.49e-06 (7.75e-07)	4.69e-06 (1.73e-06)
480(20)	3.16e-06 (4.87e-07)	4.32e-06 (1.40e-06)	2.10e-08 (1.43e-08)	7.72e-06 (9.36e-07)	1.59e-07 (5.87e-08)	6.62e-07 (1.58e-07)
525(25)	9.51e-07 (1.47e-07)	8.96e-08 (8.24e-08)	9.48e-10 (2.50e-09)	1.21e-06 (2.24e-07)	3.09e-08 (1.69e-08)	3.34e-18 (7.98e-10)
575(25)	1.97e-07 (4.57e-08)	1.14e-07 (4.61e-08)	3.47e-11 (4.73e-10)	7.59e-08 (3.16e-08)	5.29e-08 (2.44e-08)	0.00e+00 (0.00e+00)
650(50)	5.10e-08 (1.42e-08)	3.15e-08 (1.05e-08)	6.57e-11 (4.60e-10)	1.95e-08 (8.28e-09)	1.68e-08 (7.68e-09)	0.00e+00 (0.00e+00)
750(50)	1.54e-08 (8.42e-09)	1.03e-08 (6.52e-09)	0.00e+00 (0.00e+00)	2.59e-09 (2.94e-09)	2.59e-09 (2.94e-09)	2.96e-09 (3.22e-09)
Energy (MeV/u)	<sup>8</sup> Bo $d\sigma/E(b\text{ MeV/u}^{-1})$		<sup>10</sup> Bo $d\sigma/E(b\text{ MeV/u}^{-1})$		<sup>11</sup> Bo $d\sigma/E(b\text{ MeV/u}^{-1})$	
100(100)	1.53e-08 (1.09e-08)		9.38e-09 (8.04e-09)		1.33e-08 (9.98e-09)	
215(15)	5.11e-08 (4.57e-08)		3.29e-08 (3.59e-08)		4.63e-08 (4.32e-08)	
245(15)	1.17e-07 (7.72e-08)		7.56e-08 (5.89e-08)		1.03e-07 (7.13e-08)	
275(15)	3.58e-07 (1.33e-07)		2.97e-07 (1.18e-07)		3.17e-07 (1.24e-07)	
305(15)	1.27e-06 (3.86e-07)		2.58e-07 (1.47e-07)		6.58e-06 (1.59e-06)	
335(15)	3.13e-06 (2.59e-07)		5.68e-06 (2.05e-06)		6.66e-05 (7.78e-06)	
365(15)	4.17e-06 (3.83e-07)		6.95e-05 (1.69e-05)		1.41e-04 (2.77e-05)	
400(20)	1.74e-06 (1.80e-07)		4.87e-05 (5.64e-06)		7.68e-05 (6.39e-06)	
440(20)	2.93e-07 (7.61e-08)		3.99e-05 (4.04e-06)		3.47e-07 (4.45e-06)	
480(20)	7.79e-08 (5.11e-08)		2.22e-05 (4.90e-06)		2.38e-07 (1.12e-07)	
525(25)	5.27e-08 (3.83e-08)		1.86e-06 (1.40e-06)		6.97e-09 (1.26e-08)	
575(25)	0.00e+00 (0.00e+00)		0.00e+00 (0.00e+00)		2.82e-08 (2.71e-08)	
650(50)	0.00e+00 (0.00e+00)		0.00e+00 (0.00e+00)		0.00e+00 (0.00e+00)	
750(50)	0.00e+00 (0.00e+00)		0.00e+00 (0.00e+00)		0.00e+00 (0.00e+00)	

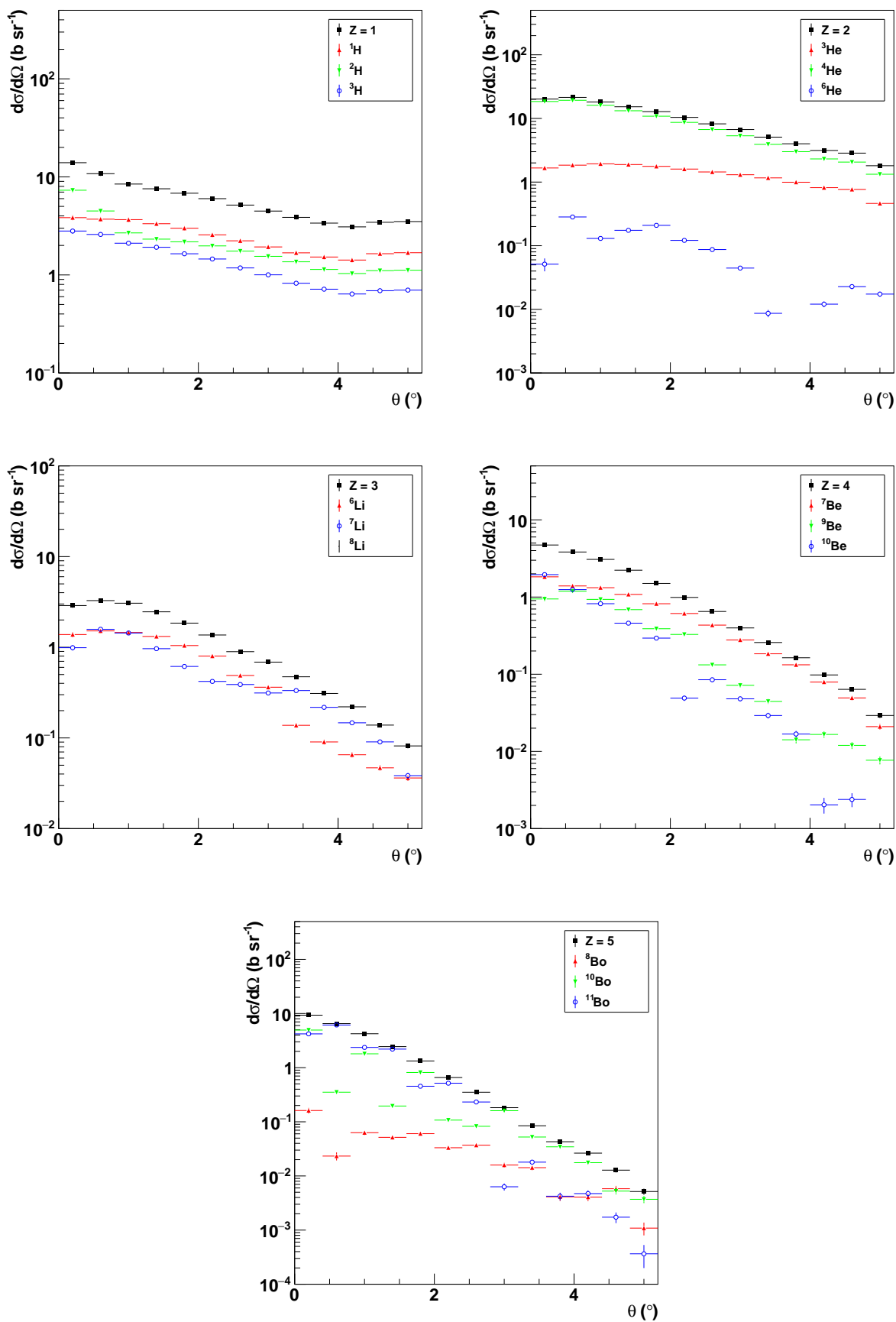


FIG. 26. Isotopes result. stat only for now: syst will be added soon

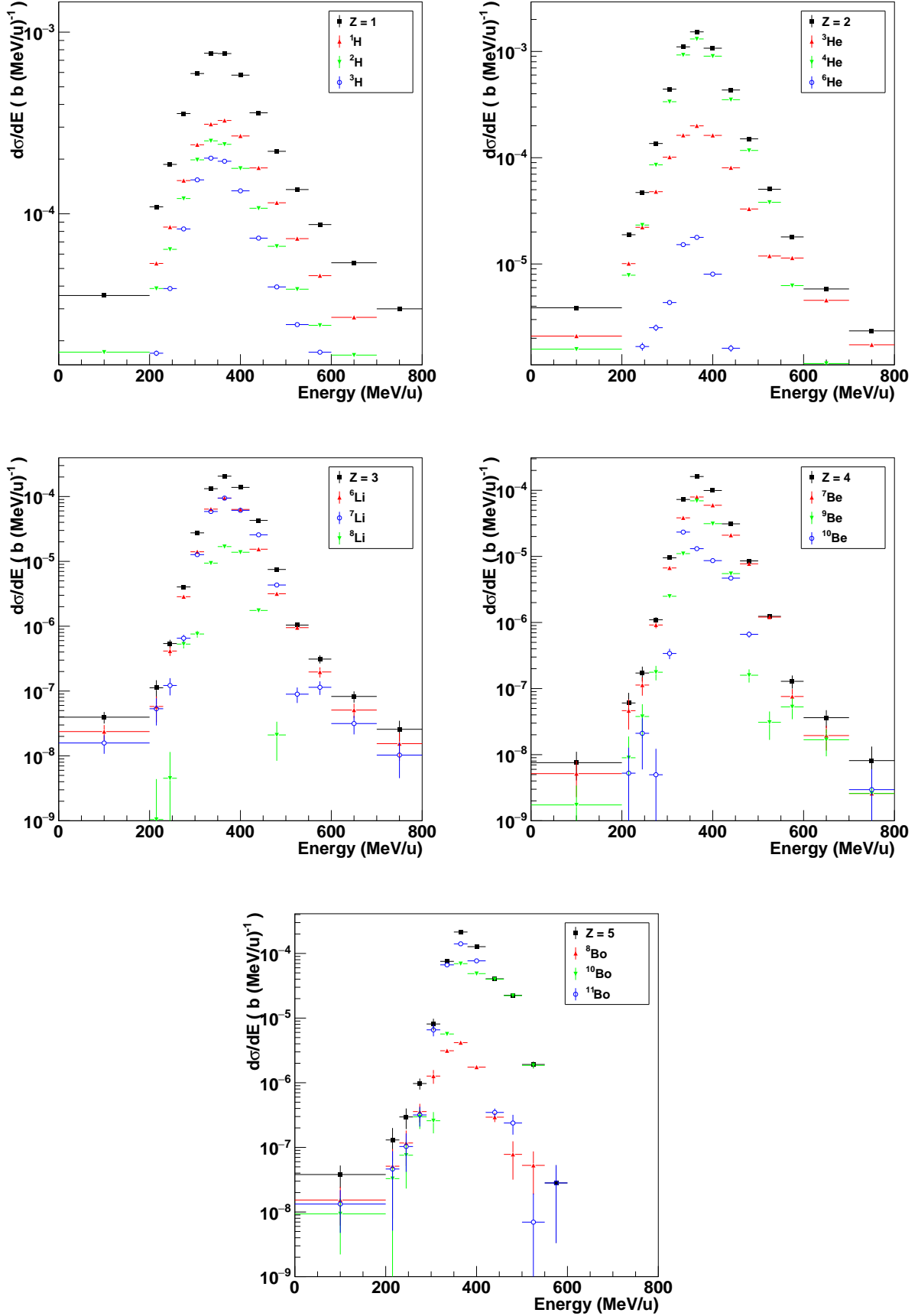


FIG. 27. Isotopes result. stat only for now: syst will be added soon